Maneuvering Predictions for Submarine Configurations

Final Report
Contract No. N-00014-97-1-0169

February 25, 2000

Submitted to:

L. Patrick Purtell
Office of Naval Research
800 North Quincy St.
Arlington, VA 22217-5660

Prepared by:

Farhad Davoudzadeh
David A. Boger
Howard J. Gibeling

Applied Research Laboratory
The Pennsylvania State University
P.O. Box 30
State College, PA 16803

20000309 045

REPORT DOCUMENTATION PAGE

Public reporting burden for this collection of information is estimated to average 1 hour per response, including the time for reviewing instructions, searching existing data sources, gathering and maintaining the data needed, and completing and reviewing the collection of information. Send comments regarding this burden estimate or any other aspect of this collection of information, including suggestions for reducing this burden, to Washington Headquarters Services, Directorate for Information Operations and Reports, 1215 Jefferson Davis Highway, Suite 1204, Arlington, VA 22202-4302, and to the Office of Management and Budget, Paperwork Reduction Project (0704-0188), Washington, DC 20503.

1. AGENCY USE ONLY (Leave Blank)	2. REPORT DATE 2/25/00	3. REPORT TYPE AND DATES COVERED Final

4. TITLE AND SUBTITLE
Maneuvering Predictions for Submarine Configurations

5. FUNDING NUMBERS
N-00014-97-1-0169

6. AUTHORS
Farhad Davoudzadeh
David Boger
Howard Gibeling

7. PERFORMING ORGANIZATION NAME(S) AND ADDRESS(ES)
Applied Research Laboratory
The Penn State University
Post Office Box 30
State College, PA 16804

8. PERFORMING ORGANIZATION REPORT NUMBER

9. SPONSORING / MONITORING AGENCY NAME(S) AND ADDRESS(ES)
Dr. L. Patrick Purtell
Office of Naval Research
800 North Quincy St.
Arlington, VA 22217-5660

10. SPONSORING / MONITORING AGENCY REPORT NUMBER

11. SUPPLEMENTARY NOTES

12a. DISTRIBUTION / AVAILABILITY STATEMENT
Unlimited

12b. DISTRIBUTION CODE

13. ABSTRACT *(Maximum 200 words)*
Under a prior research effort entitled, "Flow Around Maneuvering Appended Bodies" the NSF Engineering Research Center at Mississippi State (MSU/ERC) and the Applied Research Laboratory at The Pennsylvania State University (ARL) developed a physics-based means of predicting the maneuvering characteristics of a self-propelled, fully-appended underwater vehicle. Subsequently, a follow-on project to extend the initial capability was undertaken. This addresses many of the issues that remained at the conclusion of the original project. Specific areas being addressed include: (1) computation of flow at very high (full-scale) Reiynolds number, (2) investigation of different grid topologies, (3) turbulence models studies, (4) effective use of parallel processing, and (5) depth-changin maneuvers. Subsequently, the follow-on effort was divided into two parts to allow considereation of classified configurtions under a separate project.

14. SUBJECT TERMS

15. NUMBER OF PAGES
52

16. PRICE CODE

17. SECURITY CLASSIFICATION OF REPORT UNCLASSIFIED	18. SECURITY CLASSIFICATION OF THIS PAGE UNCLASSIFIED	19. SECURITY CLASSIFICATION OF ABSTRACT UNCLASSIFIED	20. LIMITATION OF ABSTRACT SAR

NSN 7540-01-280-5500

Introduction:

Under a prior research effort entitled "Flow around Maneuvering Appended Bodies'" the NSF Engineering Research Center at Mississippi State University (MSU/ERC) and the Applied Research Laboratory at The Pennsylvania State University (ARL) developed a physics-based means of predicting the maneuvering characteristics of a self-propelled, fully-appended underwater vehicles. Subsequently, a follow-on project to extend the initial capability was undertaken. This effort addresses many of the issues that remained at the conclusion of the original project. Specific areas being addressed include: (1) computation of flow at very high (full-scale) Reynolds number, (2) investigation of different grid topologies, (3) turbulence models studies, (4) effective use of parallel processing, and (5) Depth-changing maneuvers. Subsequently, the follow-on effort was divided into two parts to allow consideration of classified configurations under a separate project.

1. Computation of flow at very high (full-scale) Reynolds number:

To evaluate the issues involved in conducting high Reynolds number computations, a case study is set up to perform Navier-Stokes computations at a very high Reynolds number.

SUBOFF, a model scale submarine, has been one of the geometries used for the validation of the method developed in the course of the above mentioned research effort. The Reynolds number is 12 million for the experimental and computational studies performed with SUBOFF (based on body length). However, the full scale Reynolds number for submarines is about two orders of magnitudes higher than the one used for the model scale. Therefore, in the case study, a Reynolds number of 1.2 billion (based on body length) was used, corresponding to a full-scale submarine operating Reynolds number. The SUBOFF geometry with four stern appendages used for this case is shown in Figure 1. Since a grid for this case already existed, it was re-gridded to satisfy the high Reynolds requirement for resolving the boundary layer.

The near-body, high grid resolution requirement may increase the degree of difficulty for the timely creation of the grids with the currently available grid generation packages. The cell aspect ratio increases substantially and generally it is much harder to create a good quality grid. This tests the robustness of the flow solver and may increase the number of cycles required for convergence. Accurate definition of the underlying body geometry (with CAD) is also a difficult requirement. Typically the manufacturing tolerance requirements for the geometry are much larger than the high Reynolds number grid tolerance requirements, and many CAD programs are not well-suited to providing the high tolerance needed for RANS grid generation.

Figure 2 shows the comparison between the computed velocity profile (using the Baldwin-Lomax turbulence model) and the law of the wall for the Reynolds number of 12 million (based on the body length). This velocity profile is taken on the parallel mid-section of the hull. It can be seen that the velocity profile has been predicted with approximately two

grid points in the viscous sublayer. Figure 3 shows the velocity profile at the same axial location for the Reynolds number computations of 1.2 billion. The total number of grid points used for both computations, as well as grid density on the hull and appendages, are also shown in these figures. The velocity profile for the high Reynolds number computation, normal to an appendage at r/R = 0.8, where r is the radial distance from the centerline and R is the radius of the hull, is shown in Figure 4.

Figures 5 and 6 show the integrated axial force coefficient for both computations. The contribution of the viscous stresses and pressure to the axial force are also shown in these figures. It is noted that the number of cycles required to convergence has increased dramatically for the higher Reynolds number case. A better quality grid can decrease the number of cycles required to achieve convergence. This was demonstrated by MSU/ERC in a similar computation with an improved grid. The need to create good quality grids in a timely manner lead to the following study.

2. Investigation of different grid topologies

A study to improve grid quality and simplify grid generation for complex geometries was initiated under a separate propulsor analysis effort. The lessons learned from that study were applied to a submarine configuration as described below.

This study intended to investigate the implementation of alternate grid topologies, to explore ways to accelerate the grid generation process and to improve the quality of the final grid. The geometry used for this study is SUBOFF with four stern appendages. Most early versions of the flow solver UNCLE require a certain type of grid topology namely, CH-grid type. This requirement imposes restrictions on the quality of the grid and on the density of the grid points near solid surfaces; on certain geometries, an O-grid or an OH-grid may yield a better quality grid. More recent versions of the UNCLE code do not have this grid topology restriction.

For this study, two grid generation software packages were considered: EAGLEVIEW and GRIDPRO. EAGLEVIEW was used to create an H-grid around the stern appendages whereas GRIDPRO was used to create OH-grid around the hull and appendages. The EAGLEVIEW grid was generated several years ago by MSU/ERC. The commercially available GRIDGEN package is now used by ARL, since EAGLEVIEW is no longer supported.

GRIDPRO is designed to create O-grids around surfaces. The O-grid may then be surrounded by an H-grid configuration. In GRIDPRO, once the grid topology is defined, the grid generation is automatic. However, if the topology is not satisfactory GRIDPRO will not converge and therefore, will not yield a usable grid. GRIDPRO creates a large number of blocks, which with the help of a postprocessor can be reduced. These blocks are located somewhat arbitrarily relative to one another with arbitrary alignment of the computational coordinate directions that makes it difficult to distinguish the block interfaces. Therefore, a preprocessor was developed to identify the inter-block surfaces

and set up an important input file for the parallel code. Figure 7 shows the overall blocking structure used by EAGLEVIEW to create a CH-grid and the blocking structure created by GRIDPRO to generate the OH-grid. It should be noted that the block structure created by GRIDPRO is automatically created by the software from the user-defined topology, whereas with EAGELVIEW the user explicitly defines the structure. Figures 9 and 10 show the grid around an appendage in the stern region for both the H-grid and O-grid. It should be noted that the grid points around the appendage are much denser for the OH-grid than the H-grid (by approximately one order of magnitude). The first grid point off the appendage surface is 1.1×10^{-6} for the OH-grid and 4.9×10^{-5} for the H-grid, both in units of body length.

Three computations were performed to examine the grid created by the GRIDPRO for SUBOFF with four stern appendages. These computations are performed at 0, 8 and 18 degree angle of drift. Velocity profiles, taken at the mid-section of the hull, for both grid types are shown in Figures 2 and 11. It should be noted that the distribution of the grid points normal to the hull is much denser for the OH-grid than the H-grid. The viscous sublayer is defined with eight grid points for the OH-grid whereas it is defined with only two grid points for the H-grid. This high resolution with the OH-grid guarantees that the viscous stresses are well predicted.

The convergence history for the axial force coefficient is shown in Figure 12. Both cases were run with the Baldwin-Lomax model. As shown, the OH-grid takes longer to converge than H-grid. This is partly because the multi-grid scheme could not be used for the OH-grid, since the number of grid points in each block was not set to allow multi-grid. Also, the higher cell aspect ratio and near-surface resolution might reduce the convergence rate, especially in the absence of multi-grid iterations.

Further, the Baldwin-Lomax model with a search parameter of 2500 was used for the flow computation for the H-grid. The search parameter use is described in the attached publication, Appendix A. No search parameter was specified for the OH-grid computation, so that the search for F_{max} extended to the far field boundary.

The variation of the axial force coefficient versus angle of drift for the two grid topologies, CH and OH, are shown in Figure 13. The experimental data is also shown in this figure. For small angles of drift, the computation performed on the OH-grid is closer to the experimental data than the CH-grid computations. For angles of drift between 10 and 18 degrees, the CH-grid results are closer to the experimental results for negative values of angle of drift. It should be noted that the original Baldwin-Lomax turbulence model is used for the latter two calculations. A prediction using Coakley's q-ω turbulence model is also shown in the figure. Figure 13 also shows the prediction for CH-grid using Baldwin-Lomax turbulence model with the search parameter of 2500. A very good comparison with the experimental data is observed for positive values of the angle of drift. Because of the asymmetry in the experimental data (for a symmetric body), no model can predict these experimental data for both positive and negative values of the drift angle. The asymmetry in the data indicates an additional error not captured by the uncertainty bars shown. A more detailed analysis of the choice of the turbulence models on the predicted results is

given in the enclosed publication. The present results indicate the need for a systematic grid resolution study to properly quantify the grid-related errors. This must be done before a more thorough analysis of the turbulence model can be performed.

Comparison of the predicted pressure coefficients and the experimental data are shown in Figures 14 and 15. The only deviation between the experimental data and the computational results occurs at the tip of the appendage for the H-grid. This is understandable, since the tip of the appendage in this grid is "pinched" and the tip is shaped like a triangular prism, rather than being flat, which is the case with the OH-grid. Apparently, this did not lead to significant errors in the overall force and moment predictions for the captive model tests. Note that cap blocks are required for either topology to accurately capture the actual (flat) tip geometry.

Comparison of the predicted skin friction for the OH-grid with the experimental data is shown in Figure 16. Considering the magnitude of the skin friction, the prediction is very reasonable.

An important feature of a grid is its ability to capture flow features of interest in the computational domain. Figure 9 shows grid distribution around an appendage, using the H-grid created with EAGLEVIEW and the OH-grid created with GRIDPRO. As shown in this figure, grid points for the H-grid are more densely distributed downstream of the trailing edge. This OH-grid was not constructed to capture the appendage wake; therefore the H-grid solution better captures the wake and the flow aft of the trailing edge. Figures 17 and 18 show the axial-component of the velocity on the appendages at 18-degree angle of drift for the H-grid and for the OH-grid, respectively. The H-grid qualitatively predicts expected flow features such as shed vortices. Considering cases where a propulsor exists immediately downstream of the fins, these vortices will interact with the propulsor and will change the loading on the propulsor. As indicated by these figures this particular OH-grid fails to capture the flow features shown by the H-grid aft of the trailing edge. However, in the absence of experimental flow data in this region, it is not possible to make a definitive statement about the required resolution. This demonstrates the need for further work to quantify the required resolution of salient flow features needed to accurately predict propulsor side forces during maneuvering situations.

Figures 19(a)-(b) show the pressure distribution on the SUBOFF for both grid topologies at 18-degree incidence angle. Contours of pressure on a plane perpendicular to the body are also shown in these figures. It should be noted that in the H-grid case, the Baldwin-Lomax turbulence model with the search parameter of 2500 was used and in the case of the OH-grid, the search parameter is not limited. To capture the vortical structure as depicted by the H-grid computation, it might be necessary to refine the OH-grid or to implement the search parameter limitation. The computed pressure distribution in the stern region at the 18-degree drift angle for the OH-grid is shown in Figure 20.

3. Turbulence model investigation:

A modified version of the Baldwin-Lomax model has been developed, and various versions of the k-ε and q-ω models were evaluated.

A series of computations were performed to evaluate the suitability of several algebraic as well as two-equation turbulence models. The algebraic models considered are the original Baldwin-Lomax model, the Degani and Schiff variation of the Baldwin-Lomax model, and a new proposed model. Furthermore, the two-equation model of Coakley was also evaluated. For the CH-grid used, the computations demonstrate that the original Baldwin-Lomax is not suitable for the three-dimensional computations that include vortical structure away from the body. This model dissipates and distorts the vortical structures and underestimates axial and lateral forces. The modified Baldwin-Lomax model with the specified search parameter produces well-defined vortices, and the computed forces compare well with the experimental data if a suitable search parameter is used. However, obtaining the best value of the search parameter relies on trial and error; therefore, these models are not general.

A new proposed algebraic model is a more general model that does not need a search parameter and does not require prior knowledge of the location of the leeward or windward side of the hull. It preserves the structure of the vortices better than the original Baldwin-Lomax model, although not as good as when the optimal search parameter is specified. However, in its present form, it assumes that the core of the vortical structures is aligned with the centerline axis of the body. A more general extension of the model should consider alignment of the vortical structures in any direction. The two-equation model of Coakley was also considered for several computations. This model avoids any problem-specific tailoring and is able to predict the forces on the body; however, a price is paid in terms of efficiency and robustness. In addition, the eddy viscosity appears to be too high in the cores of the shed vortices, and so the vortices diffuse too quickly.

More than thirty cases were computed to study various versions of the Baldwin-Lomax model and two-equation models. A detailed description of the cases computed and the results are given in the attached paper, Appendix A.

4. Parallel Processing:

A major issue in developing parallel codes relates to load balancing among the various processors. The parallel UNCLE code is structured to run one block per processor. Therefore, proper load balancing occurs only if all the blocks in the domain have the same number of grid points. Under this constraint each processor experiences the same execution load. In practice, this assumption has some shortcomings. First, it is not always practical or even possible to split the computational domain into equally sized blocks. This is especially true when the geometry is complex and contains numerous appendages. In these situations the geometry dictates breaking the computational domain into blocks of varying sizes, resulting in a very unbalanced loading of the

processors. Second, when the number of blocks exceeds the number of available processors, it will become necessary to submit more than one block to some or all processors. In order to overcome these shortcomings, a 'relative frame' version of the parallel version of UNCLE (denoted UNCLE-REL) was modified under another project to enable submission of any number of blocks to a single processor. In this way, balanced loading can be obtained by bundling a collection of small sized blocks together and submitting them to a single processor. The total number of grid points in those blocks is constrained only by the available memory for each processor. Furthermore, in situations where the number of processors are less than the number of the blocks, the computation still can be executed, provided that sufficient memory is available.

For verification purposes a calculation was performed with the modified parallel UNCLE-REL on a flat plate with four blocks -- each set of two blocks are submitted to a single processor. The results are identical with the results obtained using an ARL serial version of the UNCLE code. In the future, it would be desirable to apply the same modifications to the more general 'clicking' version of the UNCLE code, recently obtained from MSU/ERC. This version has been rewritten using many features of FORTRAN 90 and it is substantially different from UNCLE-REL.

5. Depth-changing Maneuvers:

Two maneuvering computations are performed to investigate the depth-changing maneuvers of a fully appended submarine type vehicle. The geometry used for these computations is that of the SUBOFF. It includes: sail, sailplanes, rudders, and horizontal stern planes and an open, five bladed propulsor. It should be noted that the original SUBOFF does not include sailplanes, nor does it include a propulsor. These components are added to the original SUBOFF to (a) make the vehicle a self-propelled vehicle and (b) to resemble a real submarine with all the appendages. However, there are no experimental data available to compare with the computational simulations, but the purpose behind these calculations are to demonstrate the applicability of the method and to observe that the characteristics of the maneuvering simulations correlates to the physics of the problem.

To induce a change on the elevation of a submarine, typically the horizontal stern planes are deflected. To simulate the effects of the deflections of the sternplanes, an external vertical thrust is applied on the planes. Based on the magnitude and direction of these forces, the integrated value of the forces and moments on the whole vehicle changes. The net result leads to change in the direction of motion of the vehicle and eventually to the change in the elevation of the vehicle.

All maneuvering computations start from a periodic solution at which only the governing equations of the fluid flow are numerically solved. Once the periodic solution is achieved equations governing vehicle dynamics are iteratively solved with the flow equations to simulate the maneuver.

Two depth-changing maneuvers are performed, a rising maneuvers and a diving maneuvers.

Rising Maneuver:

The trajectory of the vehicle during the rising maneuver is shown in Fig. 21. During this maneuver, the vehicle goes through five distinct phases. (1) Straight-and-level phase that extends from t = 0.0, to t = 3.0. During this period, no external force is applied to the vehicle and it is moving forward under the thrust induced by its own propulsor. (2) Pitch-up phase extends from approximately t = 3.0 to t = 4.0. To induce the pitch-up motion on the vehicle, an external force is applied on the horizontal stern planes. The magnitude of the force and its duration is shown in the Fig. 22. (3) Straight-and-level flight phase that extends from approximately t = 4.0 to t = 4.8. The force applied on the stern plane in the phase 2 is removed, allowing the vehicle to return to the straight-and-level flight. It should be noted that since the orientation of the vehicle has been changed during the previous pitch-up phase, the vehicle will continue to move to higher elevations. (4) Pitch-down phase starts from approximately t = 4.8 to t = 5.2. At this phase of the maneuver the thrust on the horizontal stern planes are changed to induce a pitch-down maneuver.

Pressure distribution on the body of the vehicle is shown in the Figs. 21 and 23. It is worth noting the position of the stagnation point on the nose of the vehicle and compare it with its position in the pitch-up phase of the maneuver. In the pitch-up phase the location of the stagnation point is on the upper part of the nose, as expected. In the pitch-down phase of the maneuver, the location of the stagnation point moves to the opposite side on the lower part, again as physics of the problem dictates. (5) In the final phase the force applied on the stern plane in the phase 4 is removed, allowing the vehicle to return to the straight-and-level flight. From t = 5.2 to the end of the computation the vehicle travels in the straight-and-level mode again.

Fig. 22 shows the magnitude and the manner in which the applied force on the horizontal stern planes are changed. The trajectory of the location of the vehicle during the maneuver is also shown in this figure. Angular rates experienced by the vehicle during this maneuver are shown in Fig. 24. The angles of roll, pitch and yaw are shown in the Fig. 25.

Diving Maneuver:

The procedure used to simulate the diving maneuver is very similar to the procedure used during the rising maneuver, except the direction of the applied force on the horizontal stern plane.

The trajectory of the location of the vehicle and the value of the force applied on the sten plane is given in the Fig. 26. The angles and the angular rate experienced by the vehicle are given in the Figs. 27 and 28. Considering the behavior of the roll rate in both rising and diving maneuvers, it is interesting to note that the vehicle experiences a far more radical roll from side to side in the rising maneuver than in the diving maneuver. This

could be attributed to the way that the sailplanes interact with the flow in these maneuvers. In the pitch-up maneuver, sailplanes directly interact with the flow whereas in the diving maneuver, the hull obstructs the free flow of the liquid towards the sailplane and thereby inducing a far lesser fluctuation in the roll rate.

Conclusions:

A number of issues pertaining to various aspects of the maneuvering simulations are addressed. These issues involved the choice for topology, the turbulence model, coupling of the Navier-stokes equations of flow and the six-degree-of-freedom equations of motion, full scale capabilities and the applicability of the method to simulate real world maneuvering scenarios.

The investigation of grid topologies demonstrated that great care must be taken in constructing a grid to preserve wakes and vorticies downstream of appendages. The H-grid topology allows concentration of grid cells across an appendage wake in a relatively straightforward manner when the wake is closely aligned with the streamwise direction. The OH-grid topology requires more careful control of the O-block around an appendage and the surrounding H-block to achieve satisfactory wake resolution. The O-block around an appendage allows higher wall-normal resolution to be achieved with better grid quality (cell orthogonality) than with an H-block. The proper prediction of the interaction of wakes and vorticies with a propulsor is especially important in determining the steady and unsteady propulsor loads, which are very important in correctly predicting the maneuvering behavior of a vehicle.

Several turbulence models were investigated. They included the Baldwin-Lomax algebraic model and elliptic two-equation models. The study demonstrated that the original Baldwin-Lomax model is not suitable for the three-dimensional computations that include vortical structures away from the body. This model dissipates and distorts the vortical structures and underestimates axial and lateral forces. The algebraic model was modified to account for the effects of the leeward-side vortices on the underlying viscous layers. The modified Balwin-Lomax with an appropriately specified search parameter produces very well-defined vortices, and the computed forces compare well with the experimental data only if a suitable search parameter is used. Furthermore, the modified Baldwin-Lomax preserved the vorticity better than any of the two-equation models studied. This conclusion is in agreement with the results obtained by other investigators.

Computations are presented to demonstrate the capability of the flow solver to simulate very high Reynolds number (i.e., 1.2×10^9) flow over a submarine-like configuration. The computation demonstrated that the very high Reynolds number computation can be performed; however, the creation of the high-resolution grid in this case presented a challenge.

Two depth-changing maneuvering simulations were performed to demonstrate the suitability of the method. These simulations, although not compared with experiments, demonstrated the physical behavior expected from a submarine undergoing similar maneuvers. One remaining task would be to perform maneuvering computations for which experimental data exists for comparison.
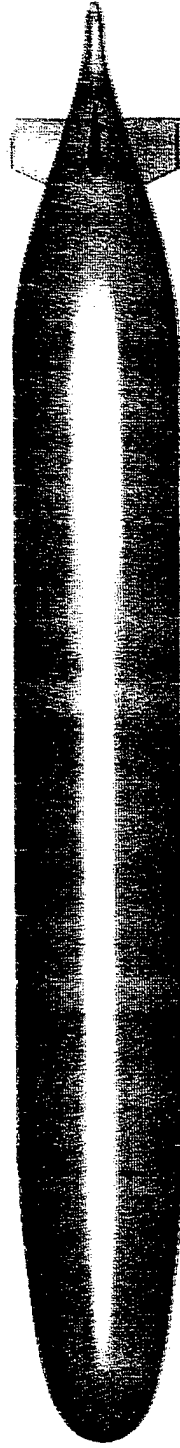
Figure 1.   SUBOFF with four stern appendages

SUBOFF WITH STERN APPENDAGES

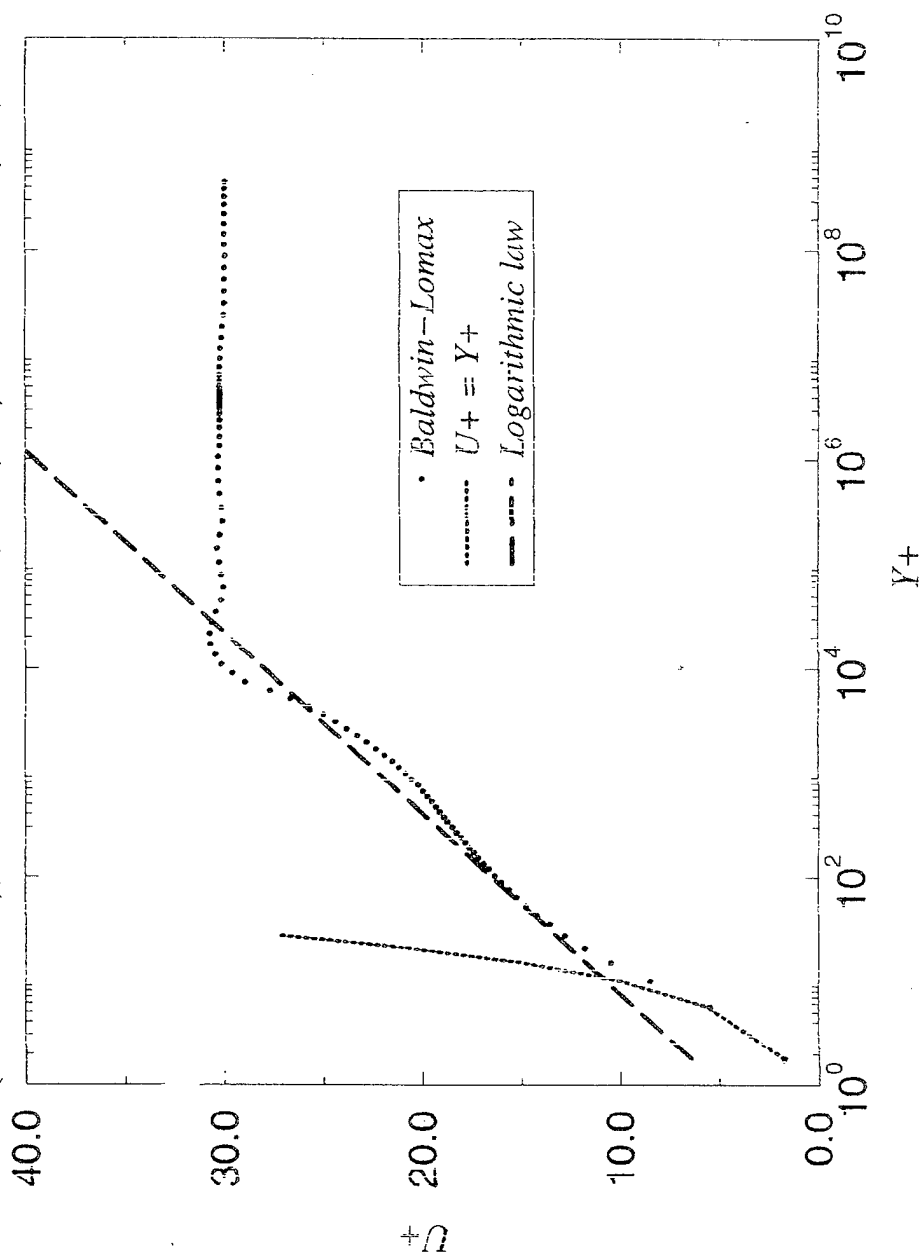Grid:(81x97x41x4), X/L = 0.5, Re = 1.2e9, ds/L(hull) = 6.4e-8, ds/L(fins) = 4.2e-6

Figure 2.   Velocity profile on the hull for CH-grid; $Re_L = 1.2 \times 10^7$

SUBOFF WITH STERN APPENDAGES

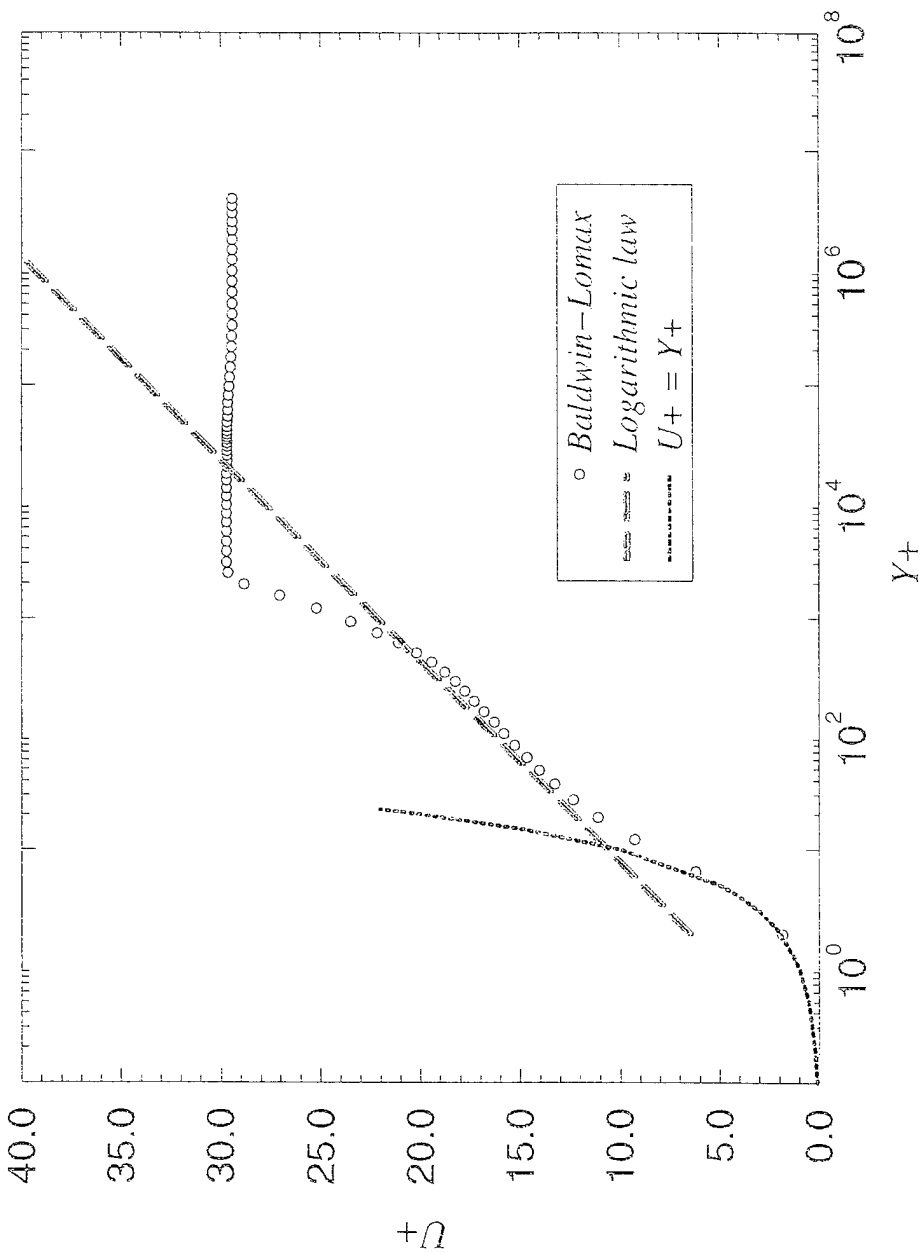H Grid:(81x73x31x4), X/L = 0.5, Re = 1.2e7, ds/L(hull) = 8.6e-6, ds/L(fins) = 4.9e-5

Figure 3. Velocity profile on the hull for CH-grid; $Re_L = 1.2 \times 10^9$

SUBOFF WITH STERN APPENDAGES, U+ vs Y+ on the fins

Grid:(81x97x41x4), X/L = 0.89, r/R = 0.80 , Re = 1.2e9, ds/L(hull) = 6.4e−8, ds/L(fins) = 4.2e−6
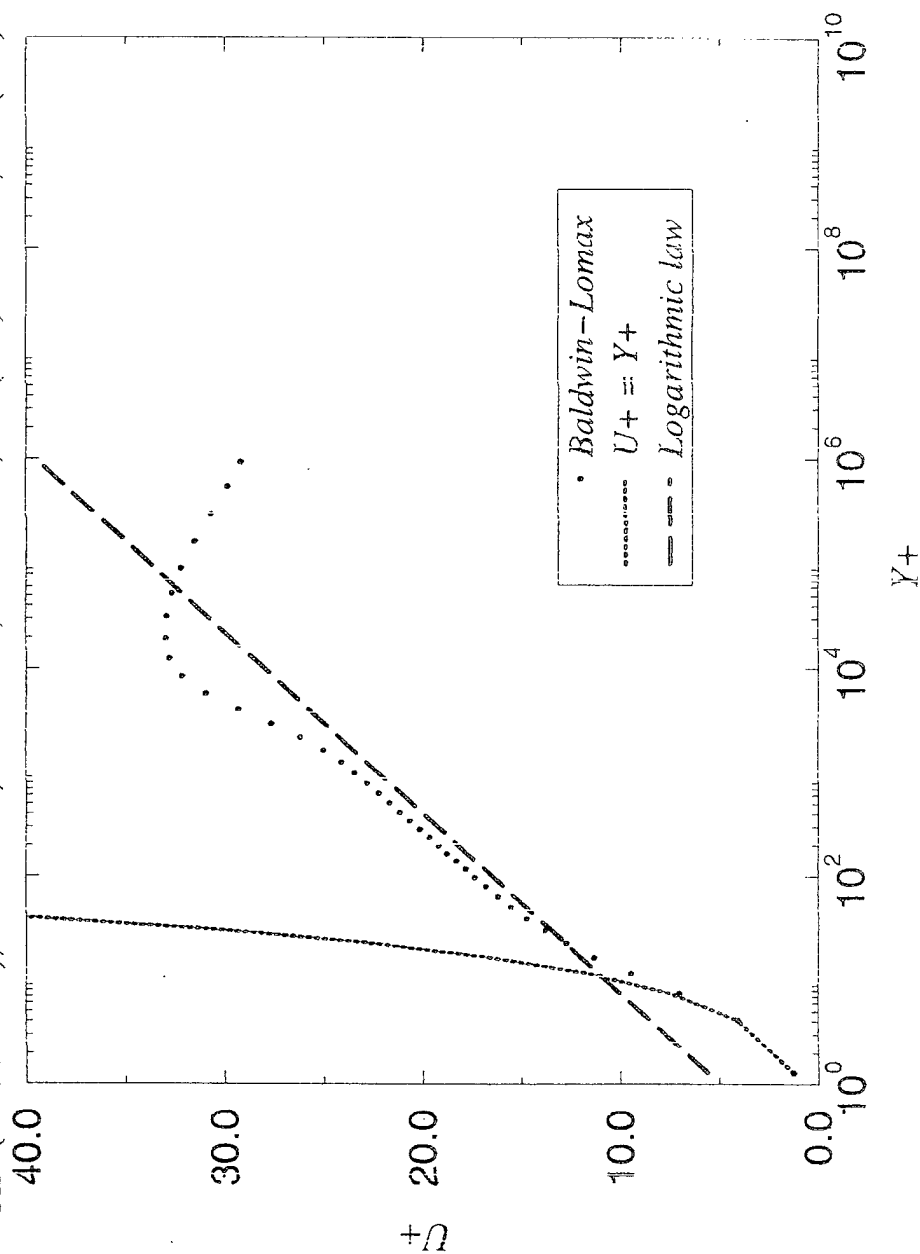
Figure 4.   Velocity profile on a stern appendage for CH-grid; $Re_L = 1.2 \times 10^9$
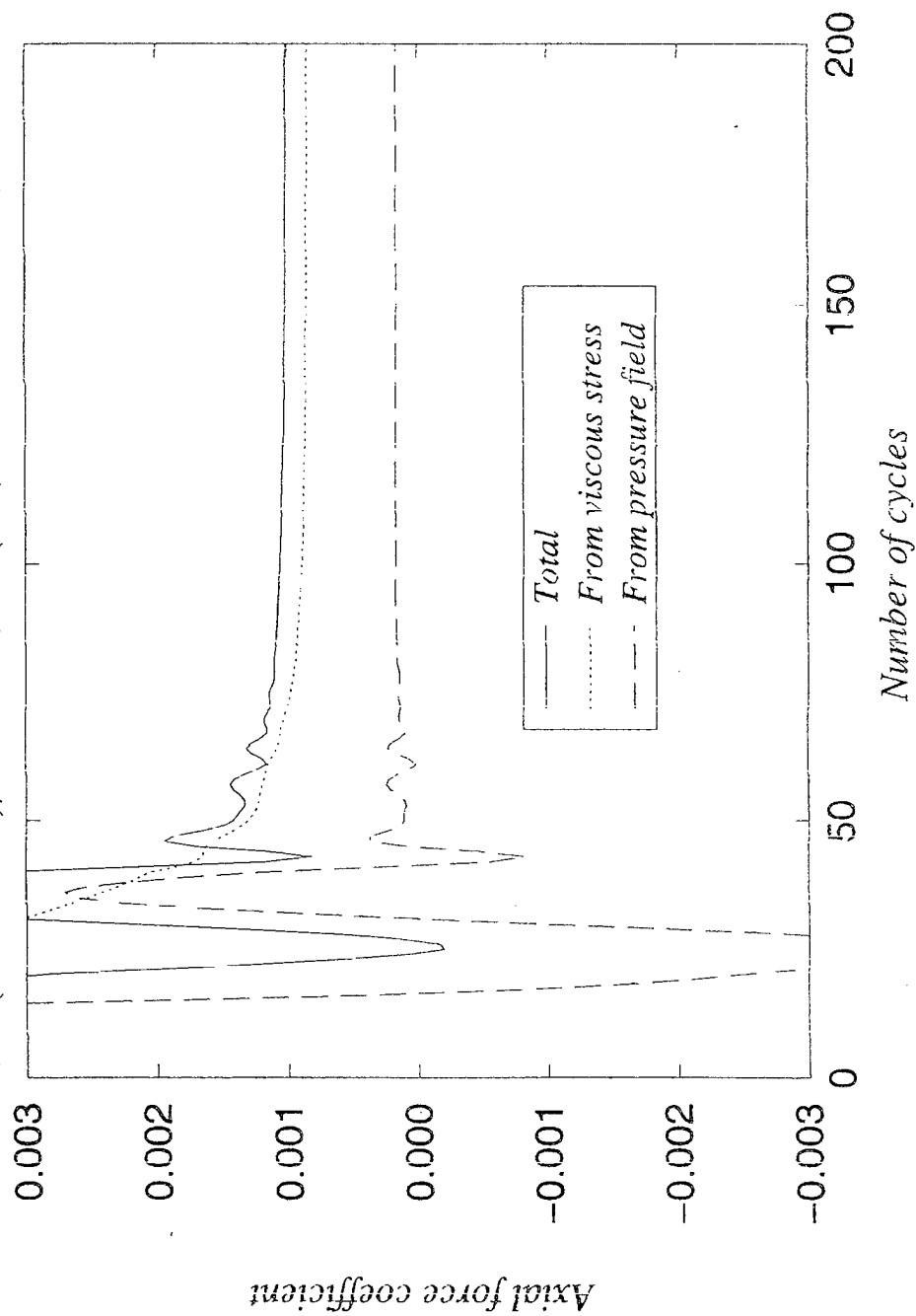
Figure 5. Convergence history for axial force coefficient; $= Re_L \, 1.2 \times 10^7$

SUBOFF WITH STERN APPENDAGES AT 0.0 DEGREE ANGLE OF DRIFT

Grid:(81x97x41x4), Re = 1.2e9, ds/L(hull) = 6.4e−8, ds/L(fins) = 4.2e−6
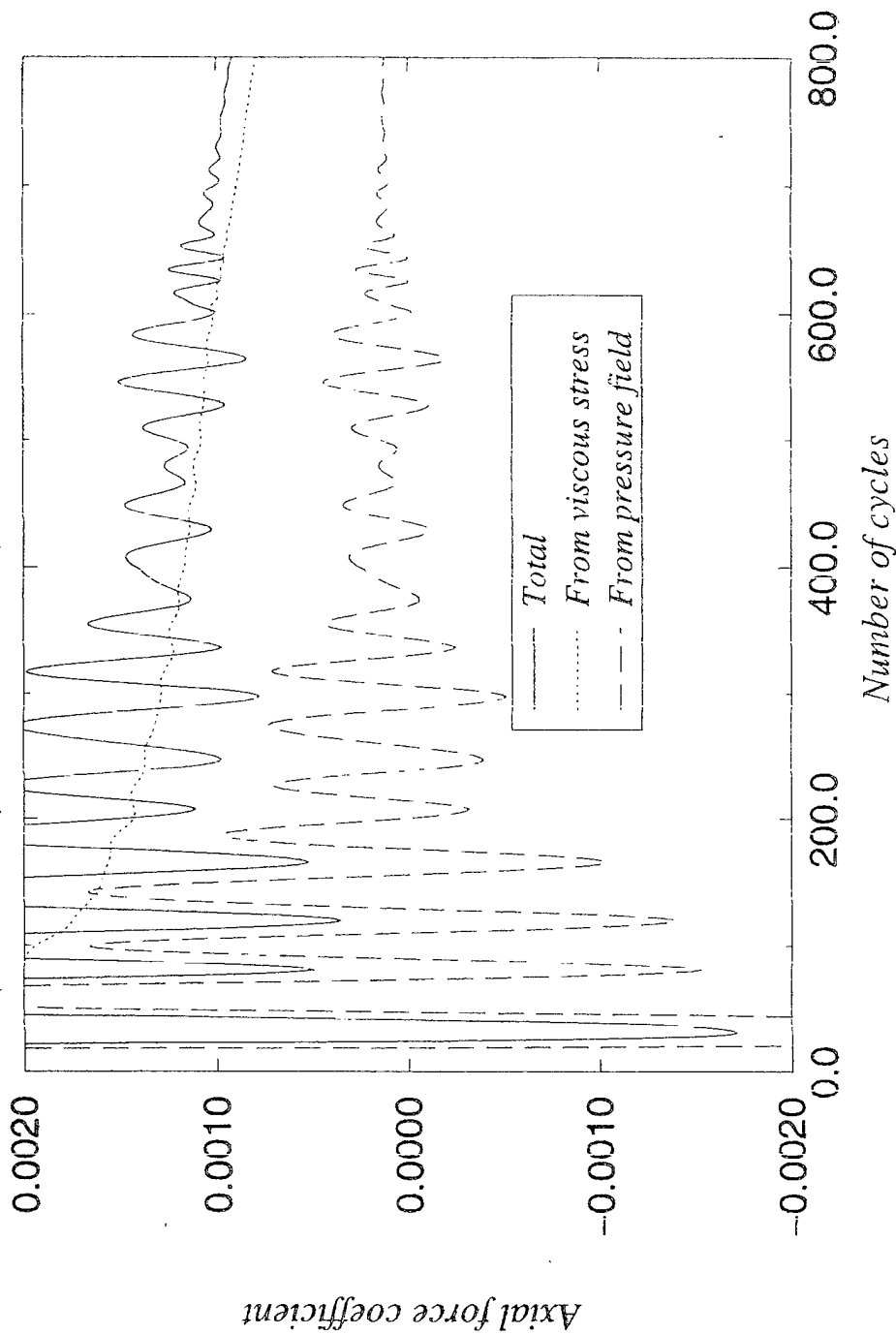
Figure 6. Convergence history for axial force coefficient; $= Re_L$ 1.2×10^9
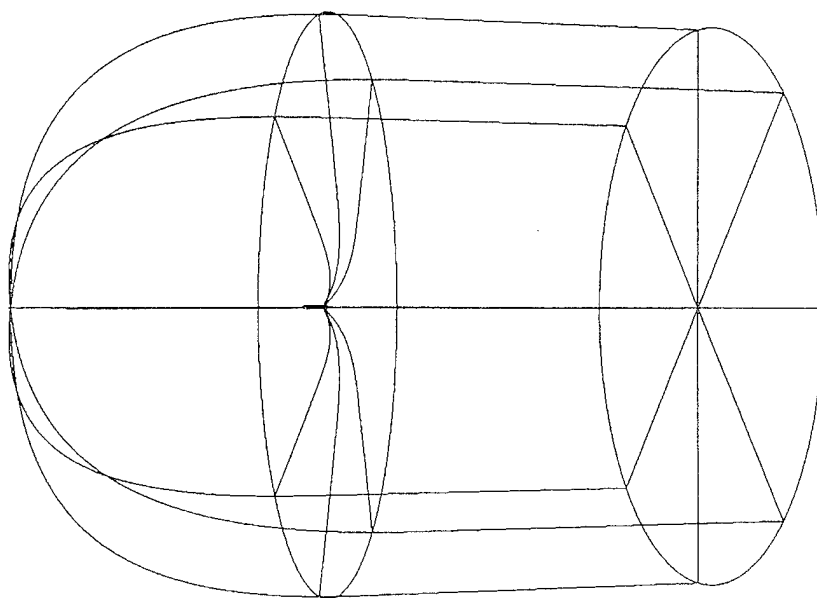
(a) CH-grid
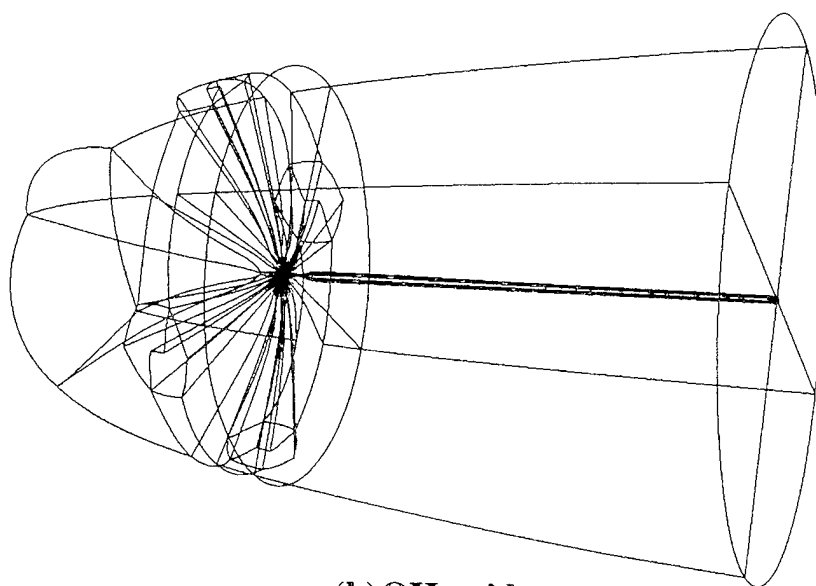
(b) OH-grid

Figure 7.   Overview of block structure for
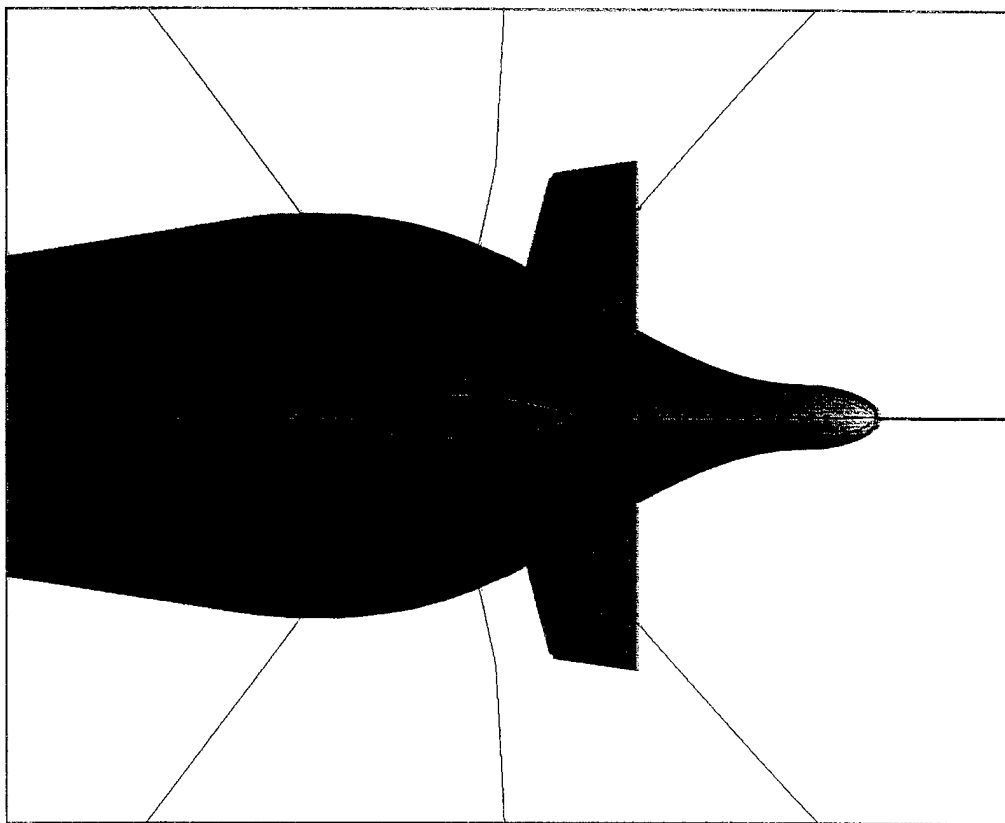
(a) CH-grid (EAGLEVIEW)
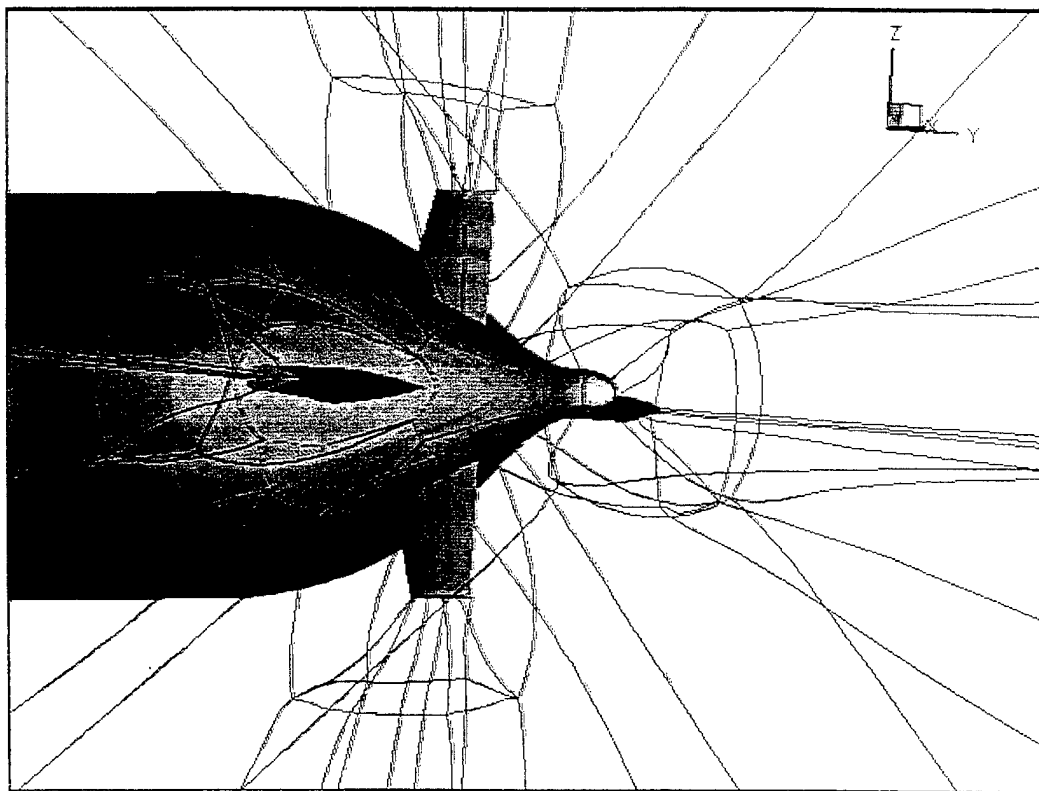
(b) OH-grid (GRIDPRO)

Figure 8.   Block structure in the stern region:
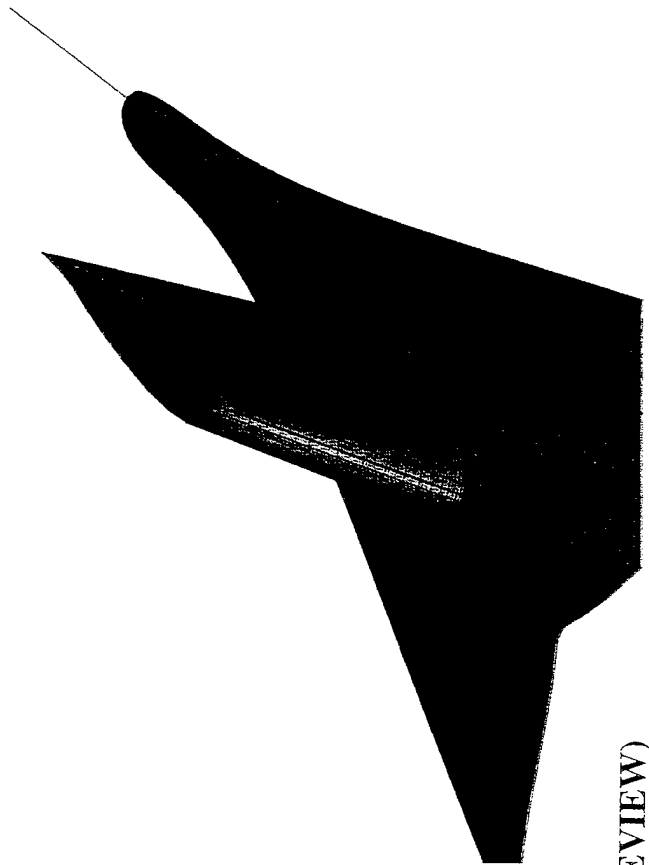
(a) H-grid (EAGLEVIEW)
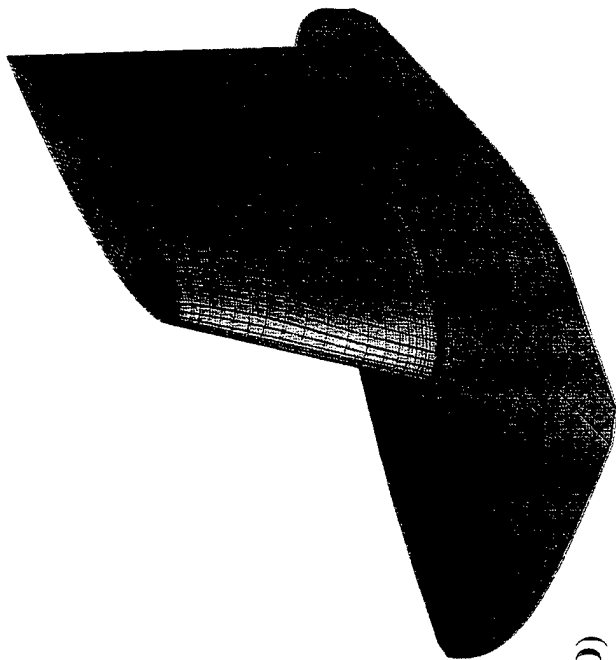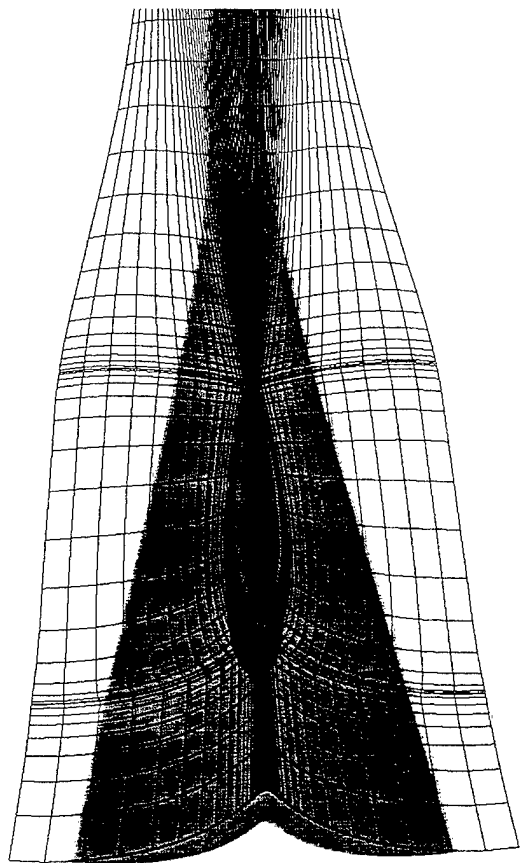
(b) OH-grid (GRIDPRO)
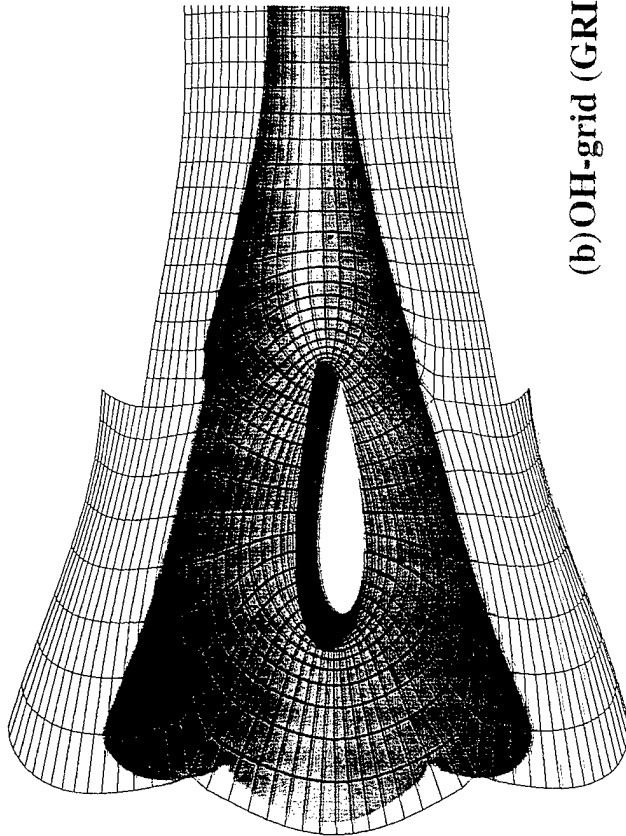
Figure 9.   Grid around a stern appendage:
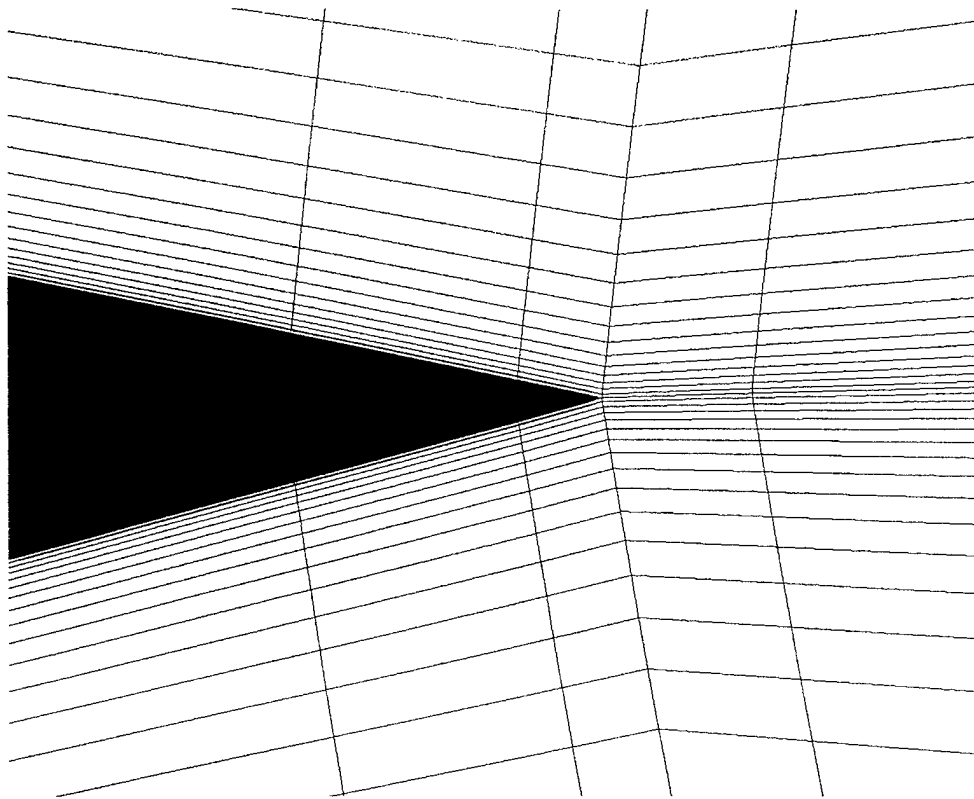
(a) H-grid
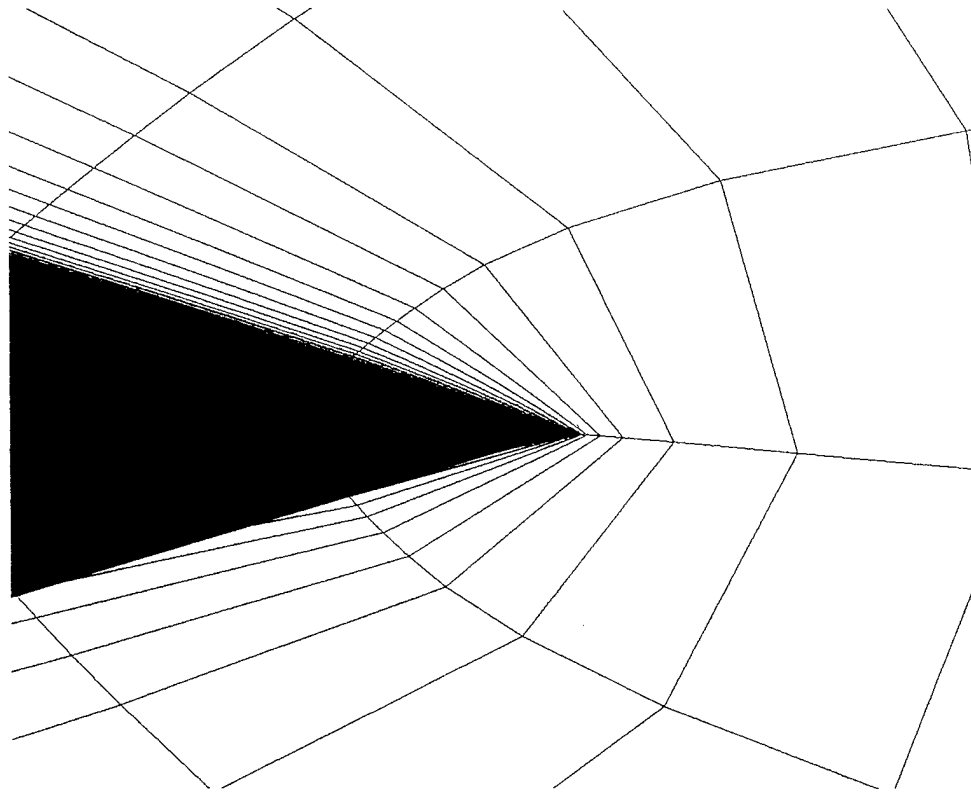
(b)OH-grid

Figure 10.   Stern appendage trailing edge grid:

SUBOFF WITH STERN APPENDAGES

OH–Grid: X/L = 0.5, Re = 1.2e7, ds/L(hull) = 1.1e–6, ds/L(fins) = 1.6e–6
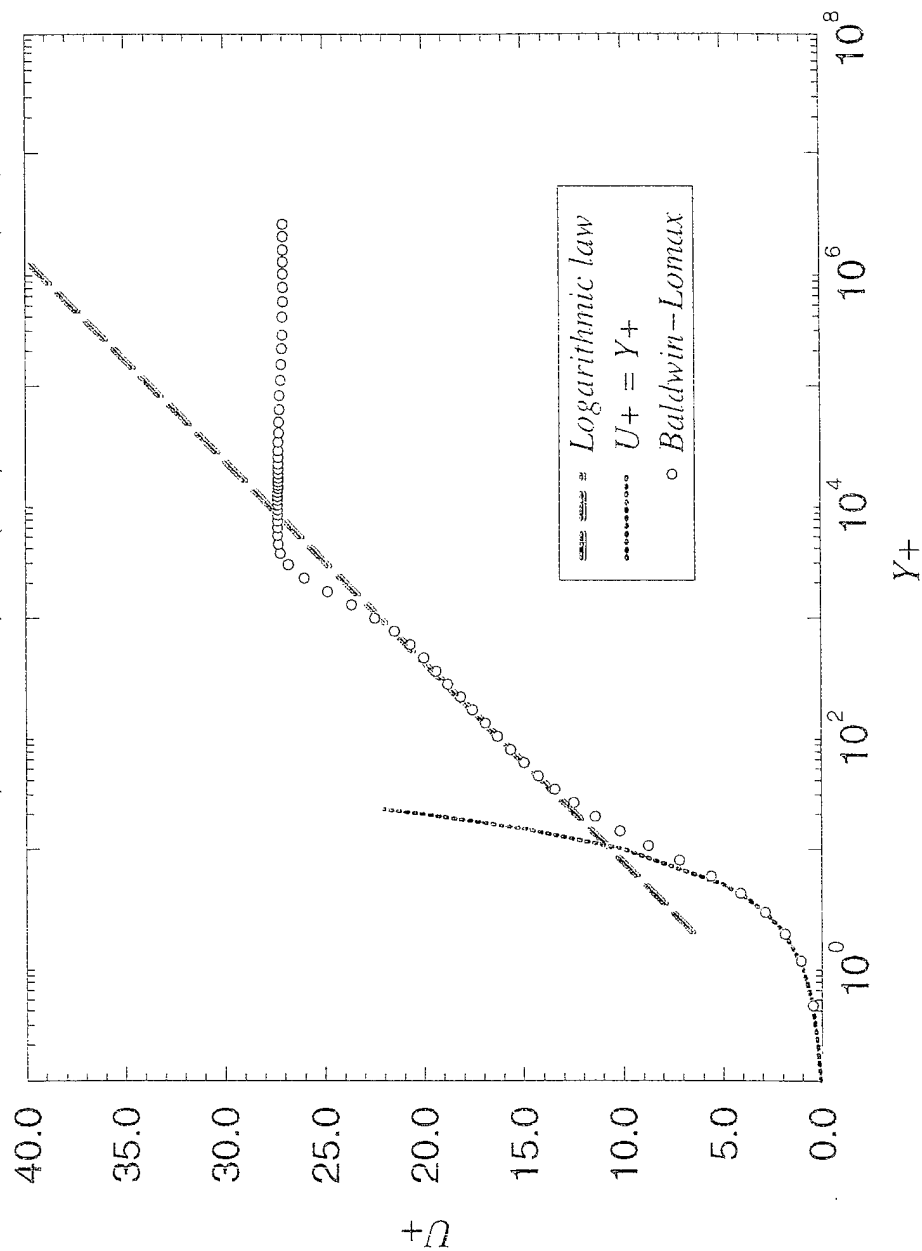
Figure 11.   Velocity profile for OH-grid; $Re_L = 1.2 \times 10^7$

SUBOFF WITH STERN APPENDAGES AT 0.0 DEGREE ANGLE OF DRIFT

Axial force convergence history for CH-grid and OH-grid, Re = 1.2e7
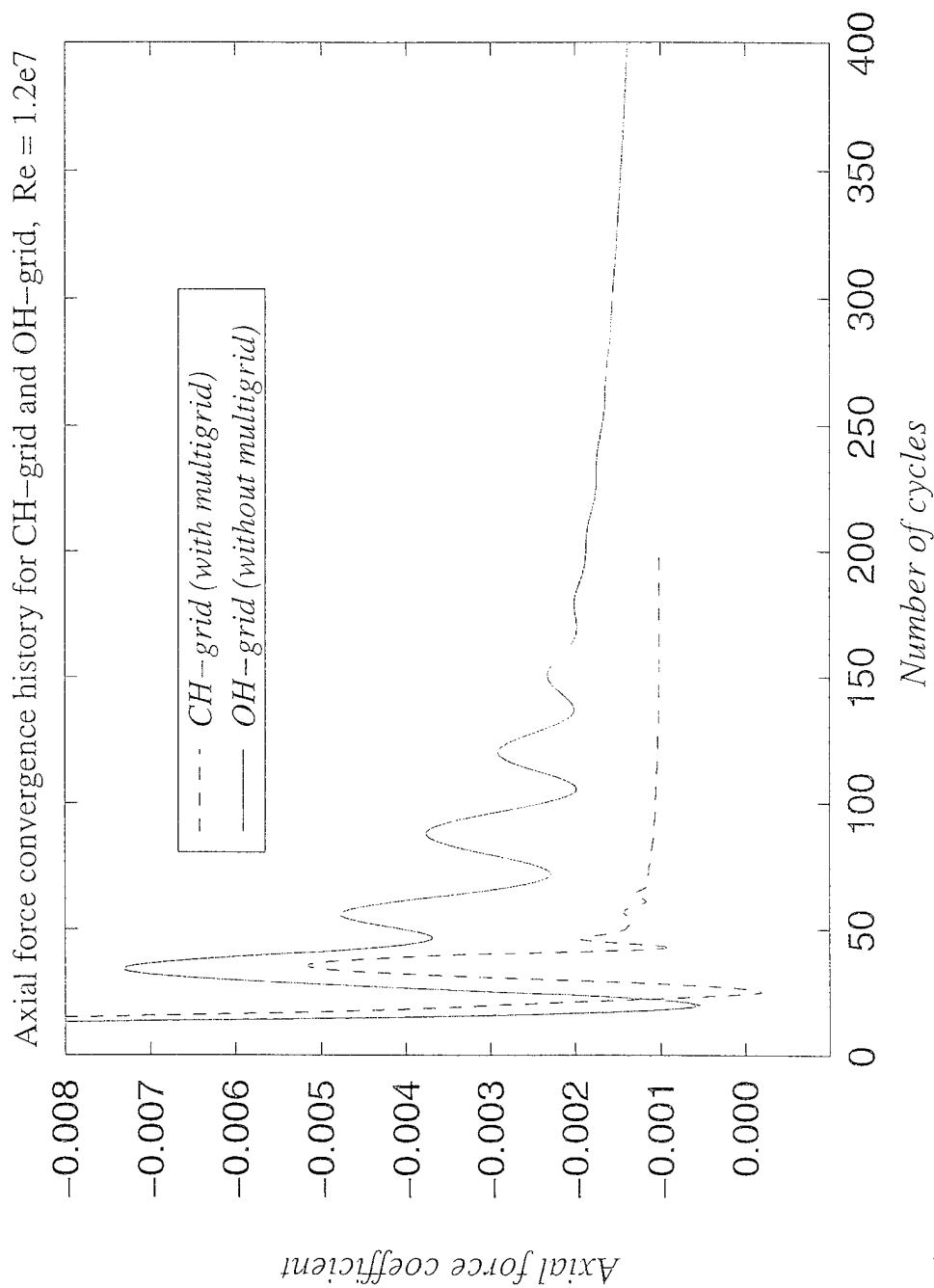
Figure 12.   Convergence history comparison for axial force coefficient;
$Re_L = 1.2 \times 10^7$

SUBOFF with stern appendages

Prediction of axial force coefficient

Legend:
- ○——○ Experimental data
- □------□ Computational using original Baldwin–Lomax, CH–grid
- △ Computational using original Baldwin–Lomax, OH–grid
- ▼ Computational using q–w (Coakley) model, OH–grid
- ◆ Computational with search parameter = 2,500, CH–grid

Axial force coefficient (vertical axis):
-6.0e–04, -8.0e–04, -1.0e–03, -1.2e–03, -1.4e–03

Angle of drift (horizontal axis):
-20.0, -10.0, 0.0, 10.0, 20.0
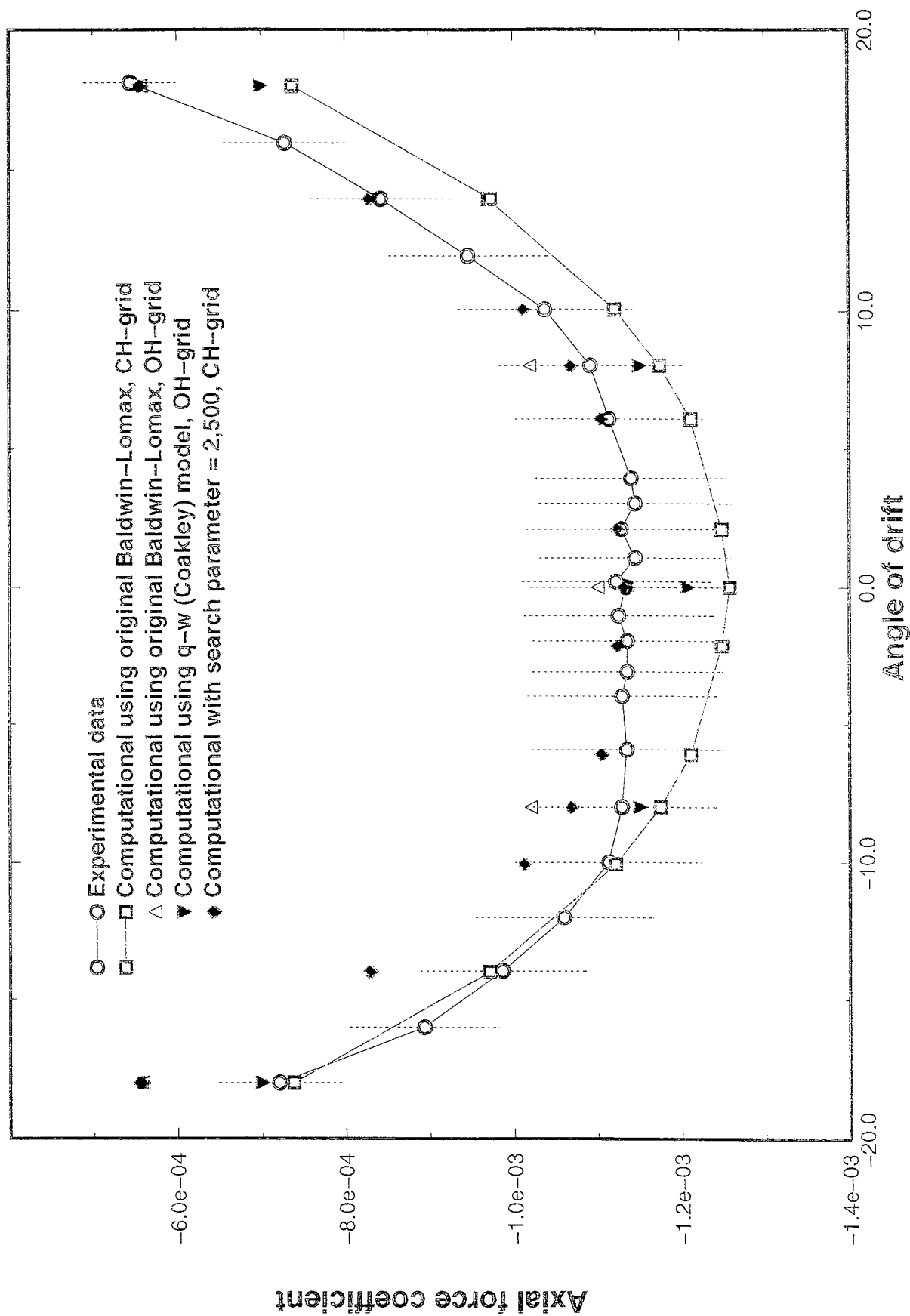
Figure 13. Axial force coefficient versus angle of drift

SUBOFF Bare Hull + 4 Stern Appendages at 0° Angle of Attack (OH grid)
Pressure Coefficient on the Stern Appendages
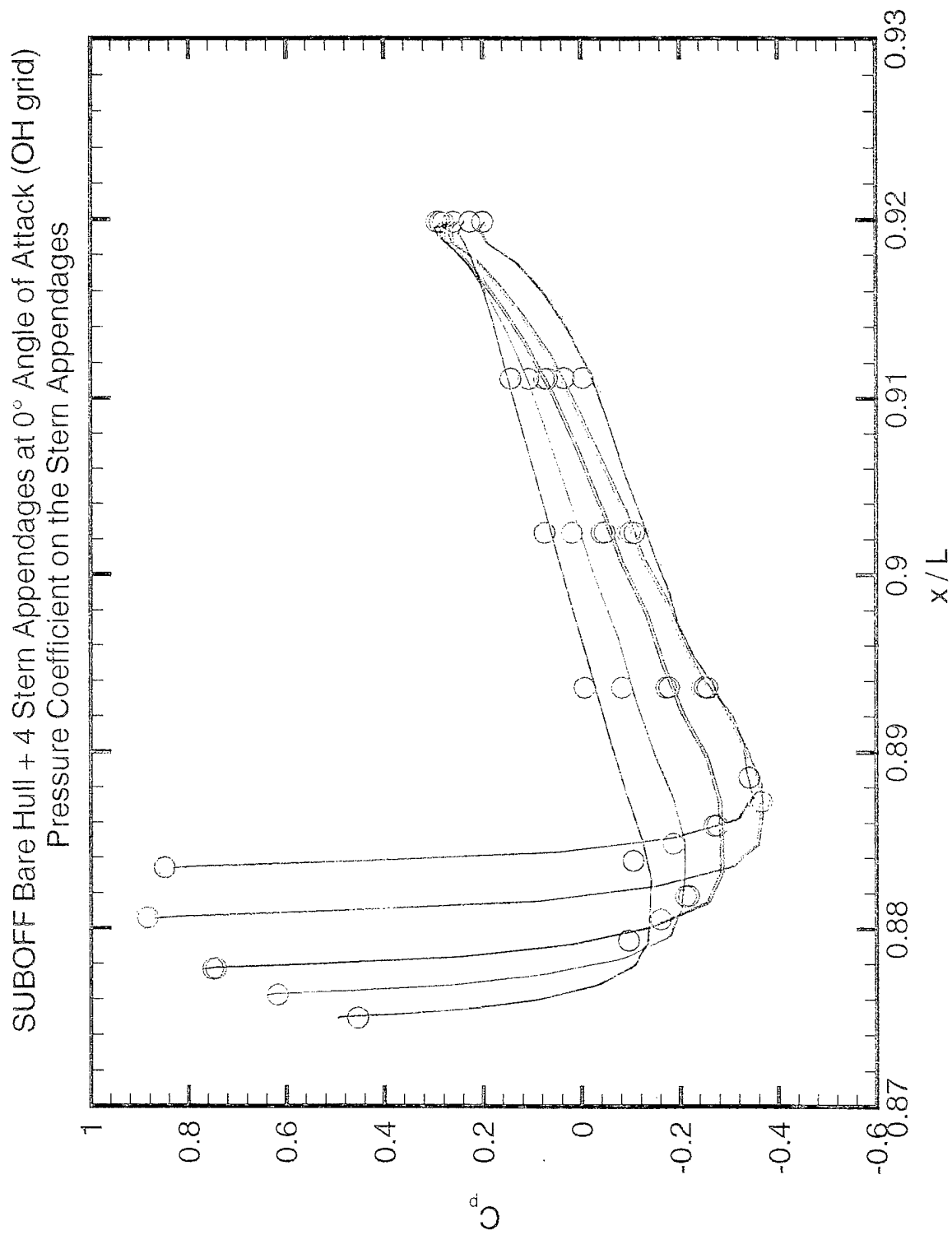
Figure 14.   Pressure coefficient on the stern appendages for the OH-grid

SUBOFF Bare Hull + 4 Stern Appendages at 0° Angle of Attack (CH-grid)
Pressure Coefficient on the Stern Appendages
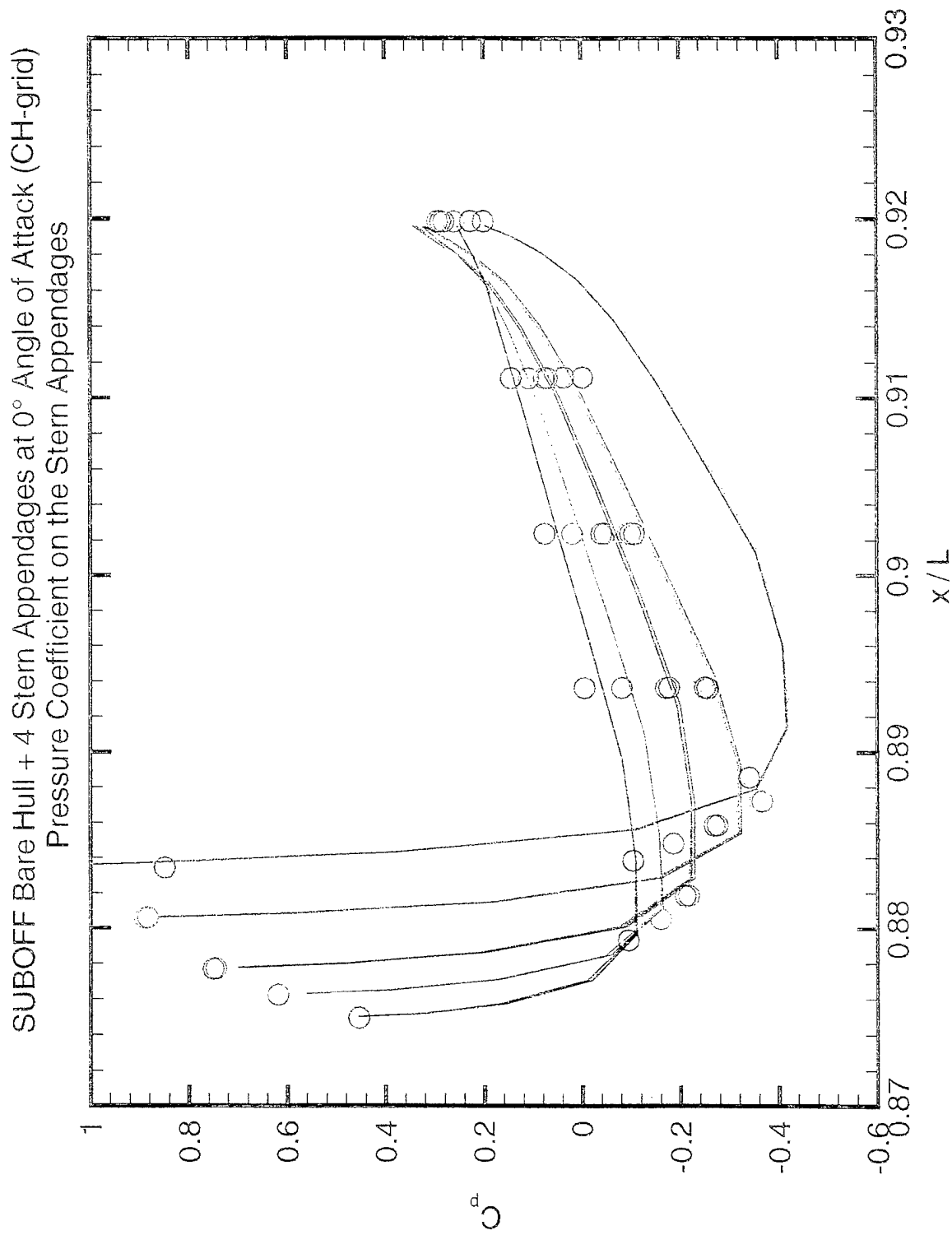
Figure 15. Pressure coefficient for the CH-grid

SUBOFF Bare Hull + 4 Stern Appendages at 0° Angle of Attack (OH grid)
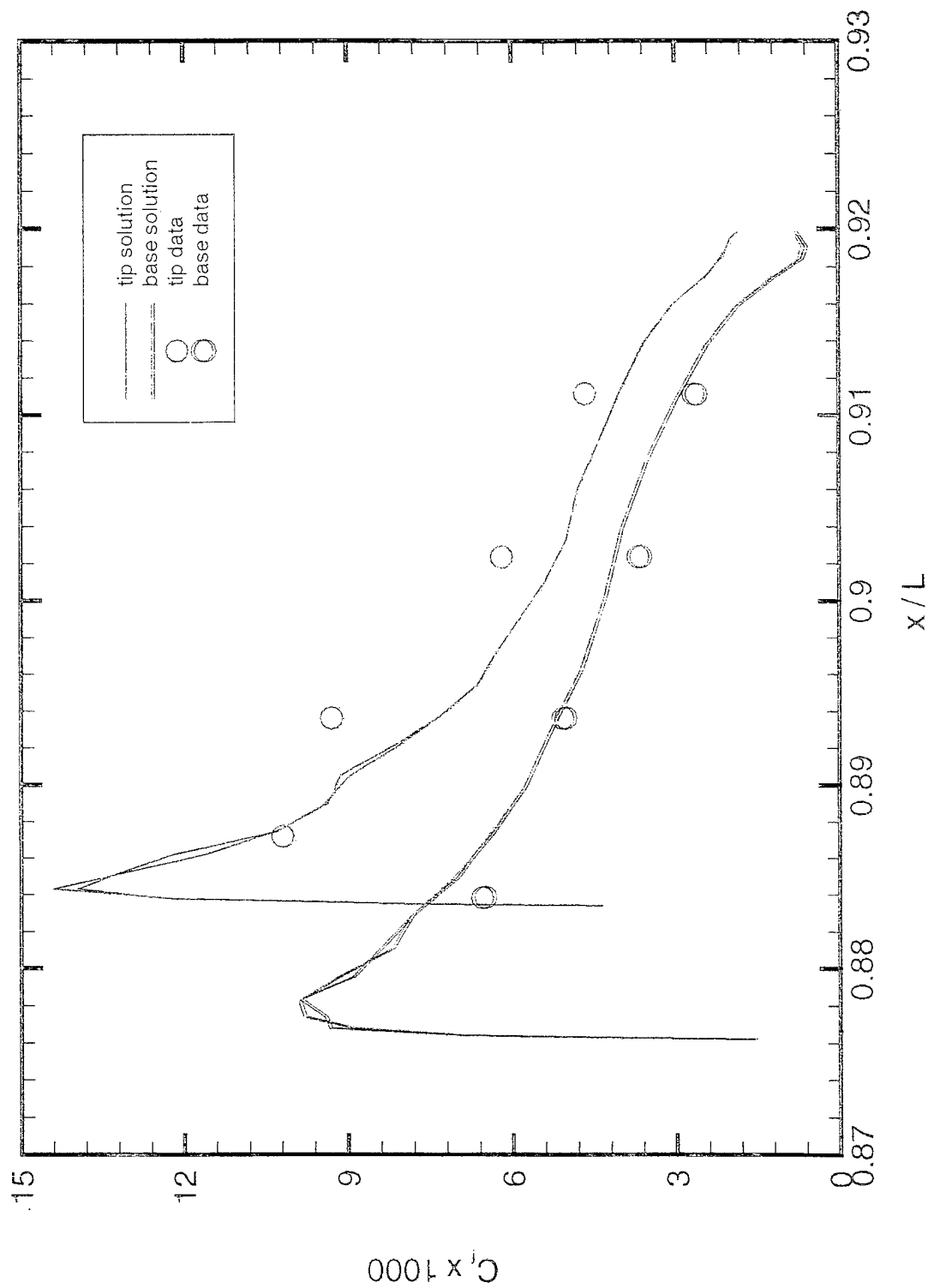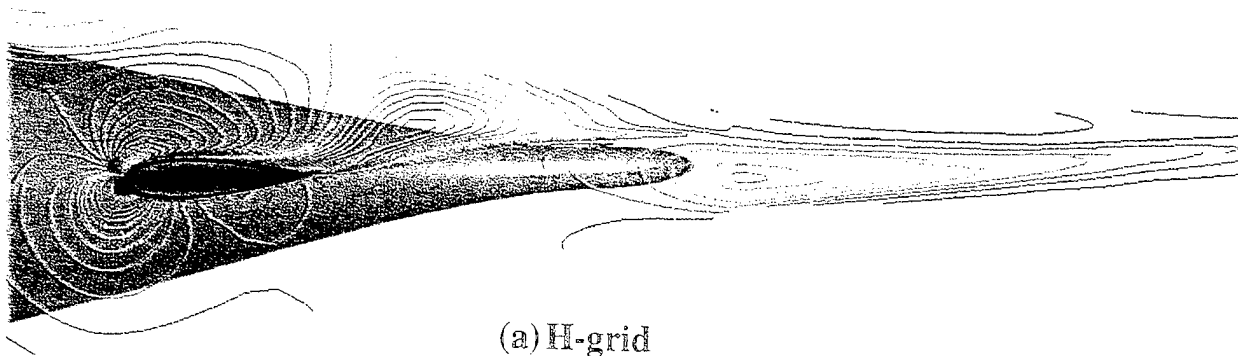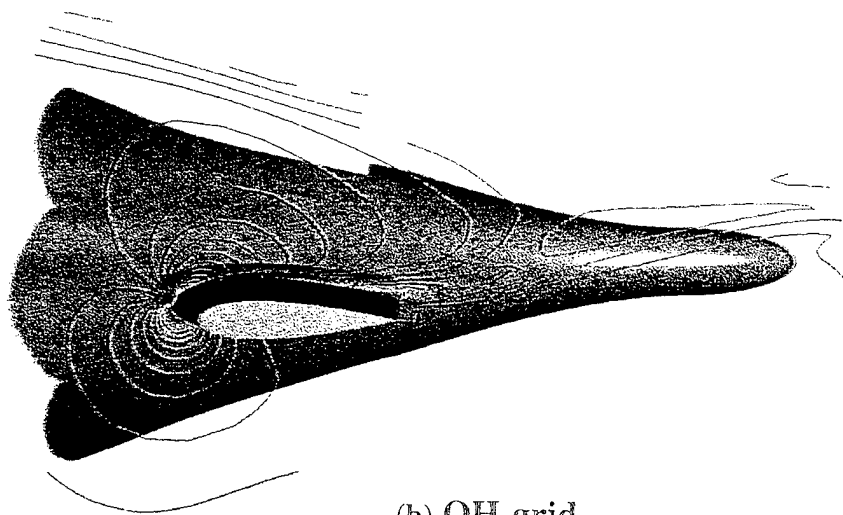Skin Friction Coefficient on the Stern Appendages

Figure 16. Skin friction on the stern appendages for OH-grid

(a) H-grid

(b) OH-grid

Figure 17.   Flow near the stern appendage at 18° angle of drift;
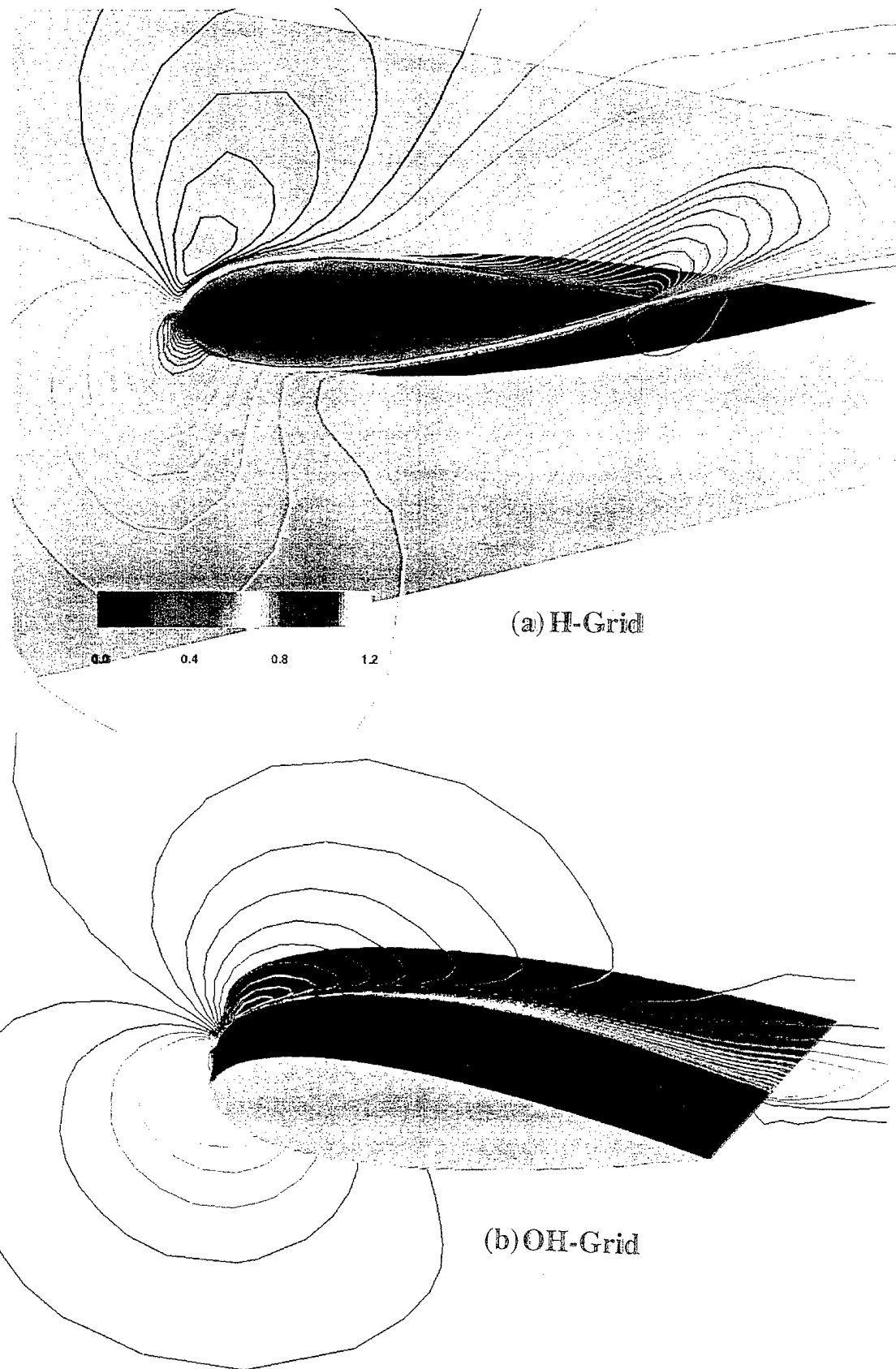contours of x-component of velocity

(a) H-Grid

0.0   0.4   0.8   1.2

(b) OH-Grid

Figure 18.   Contours of x-component of velocity around the stern appendage
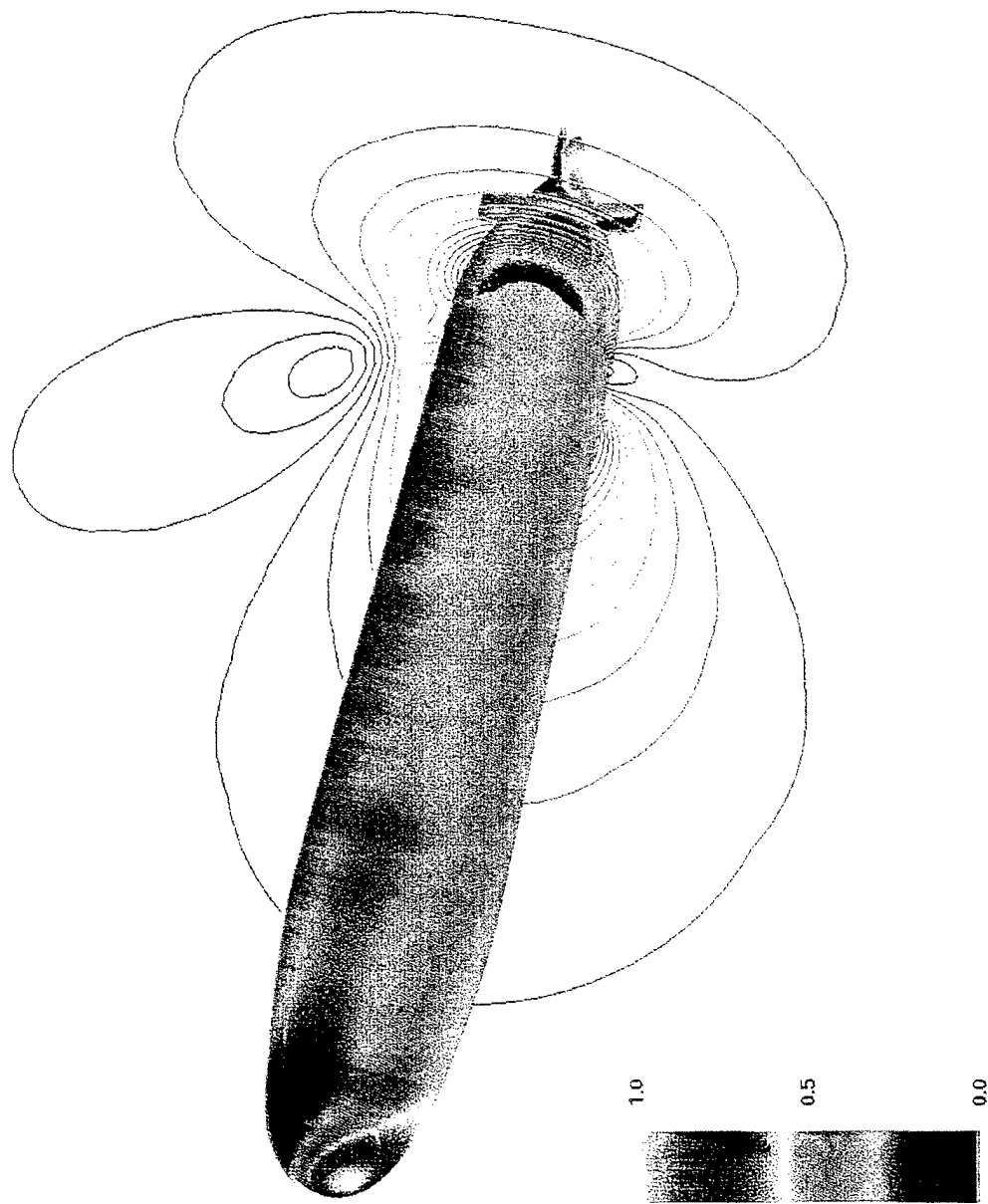
0.05
−0.01
−0.06
−0.12

0.0　　　　0.5　　　　1.0
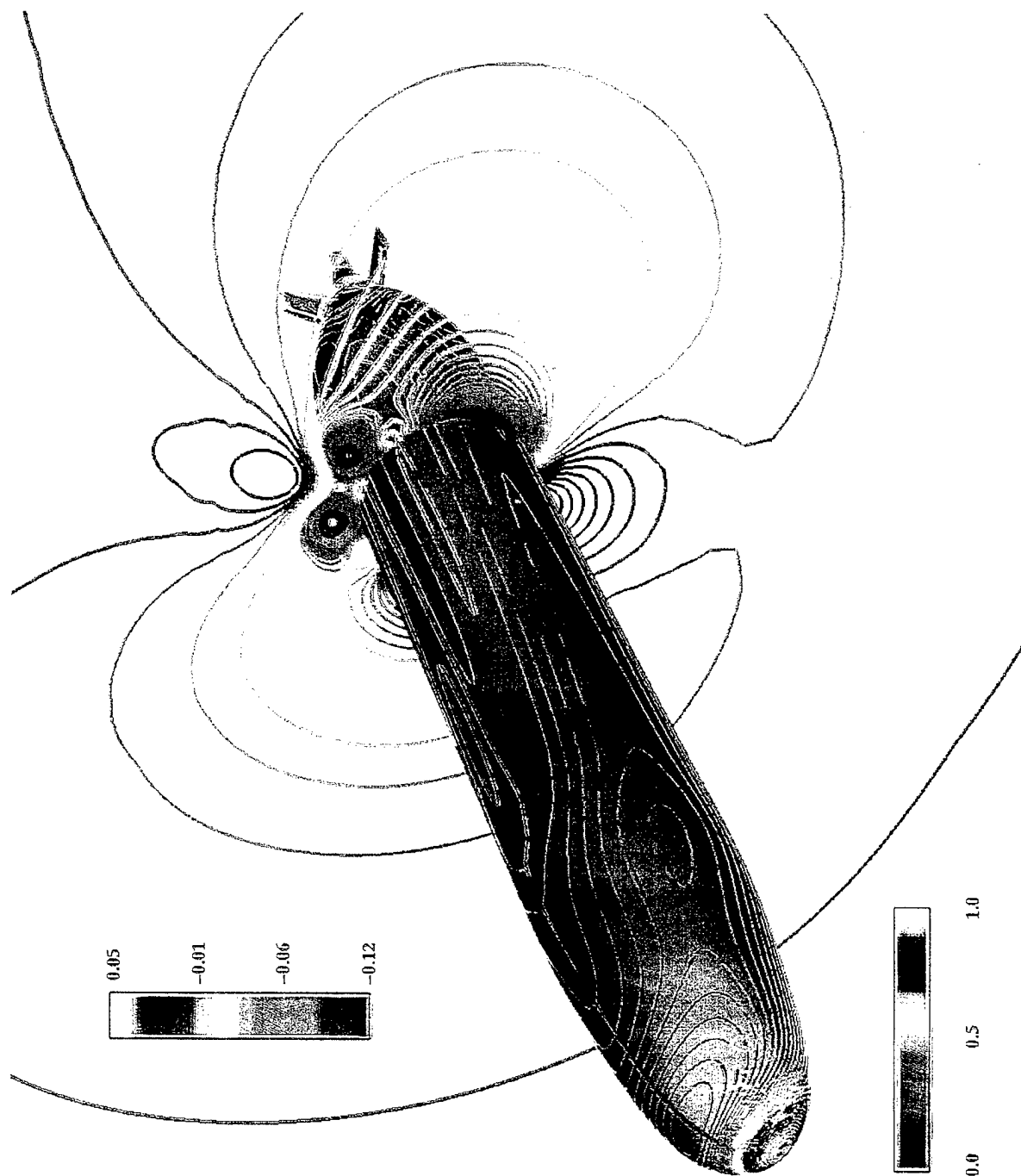
Figure 19. Pressure distribution on SUBOFF at 18° angle of incidence

(a) H-grid

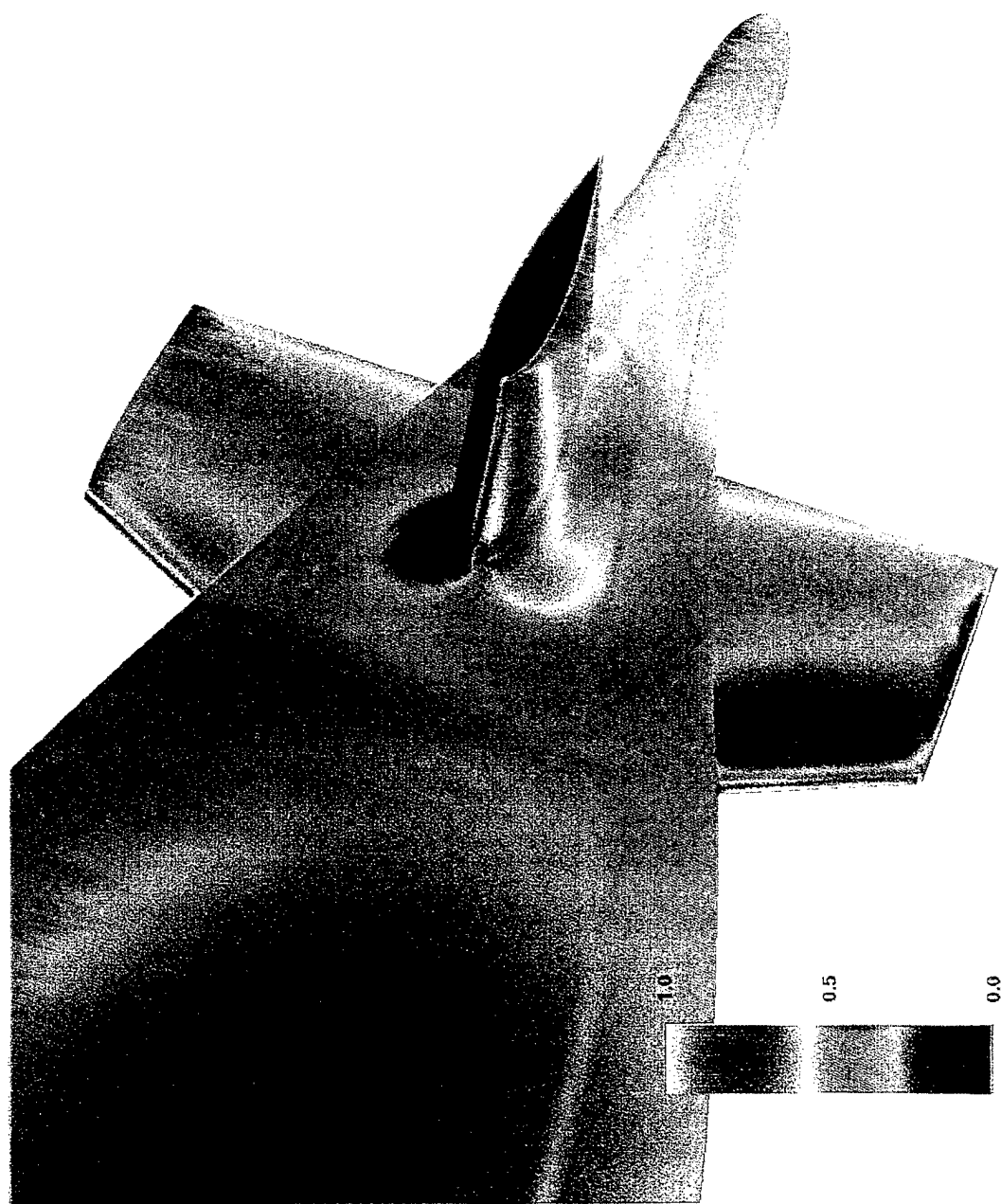Figure 19.　Pressure distribution on SUBOFF at 18° angle of incidence

(b)OH-grid

Figure 20.   Pressure distribution in the stern region of SUBOFF, OH-grid

Depth–changing maneuver with fixed control surfaces
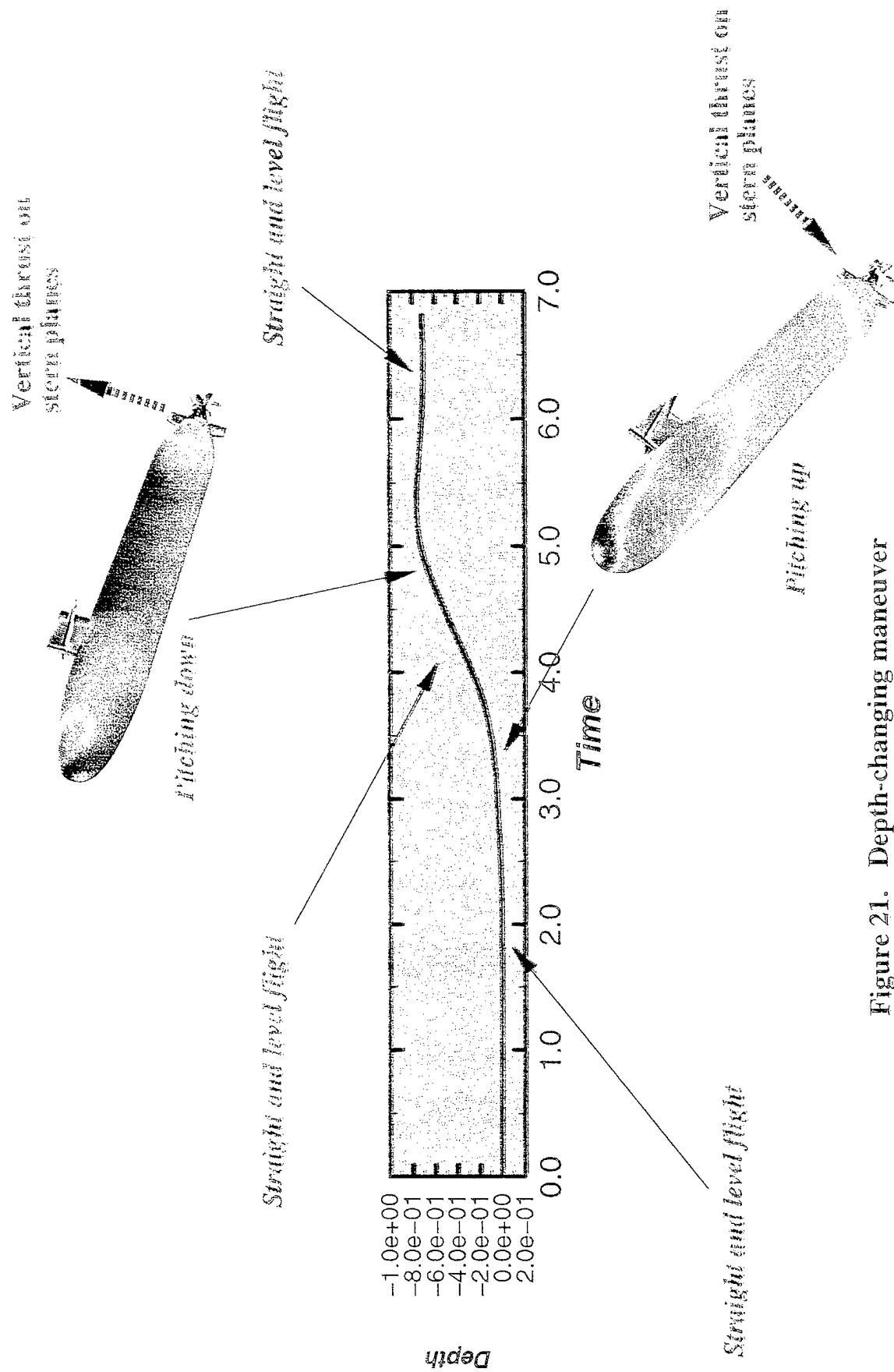## (fully–appended submarine with a rotating propulsor)

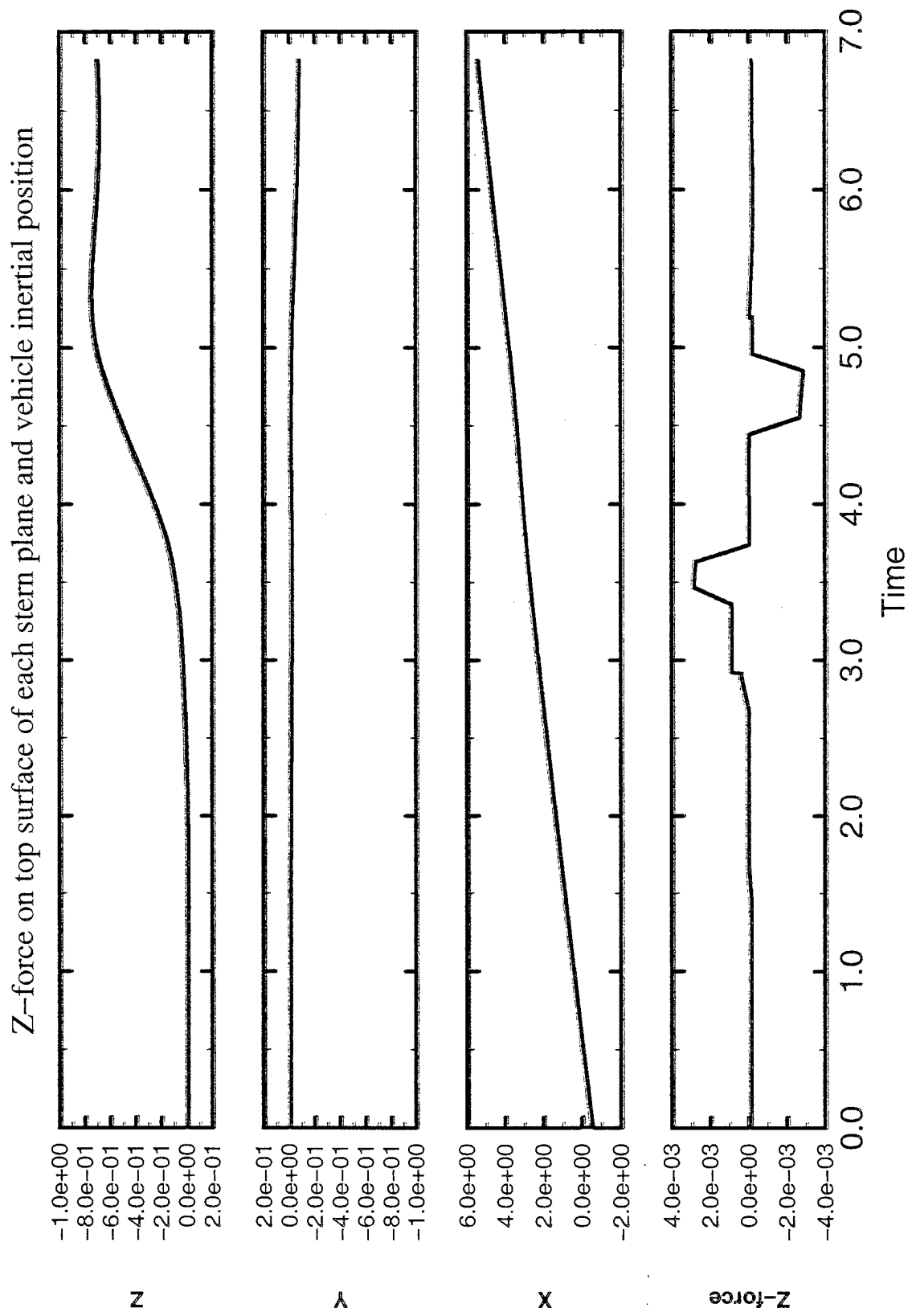Figure 21.   Depth-changing maneuver
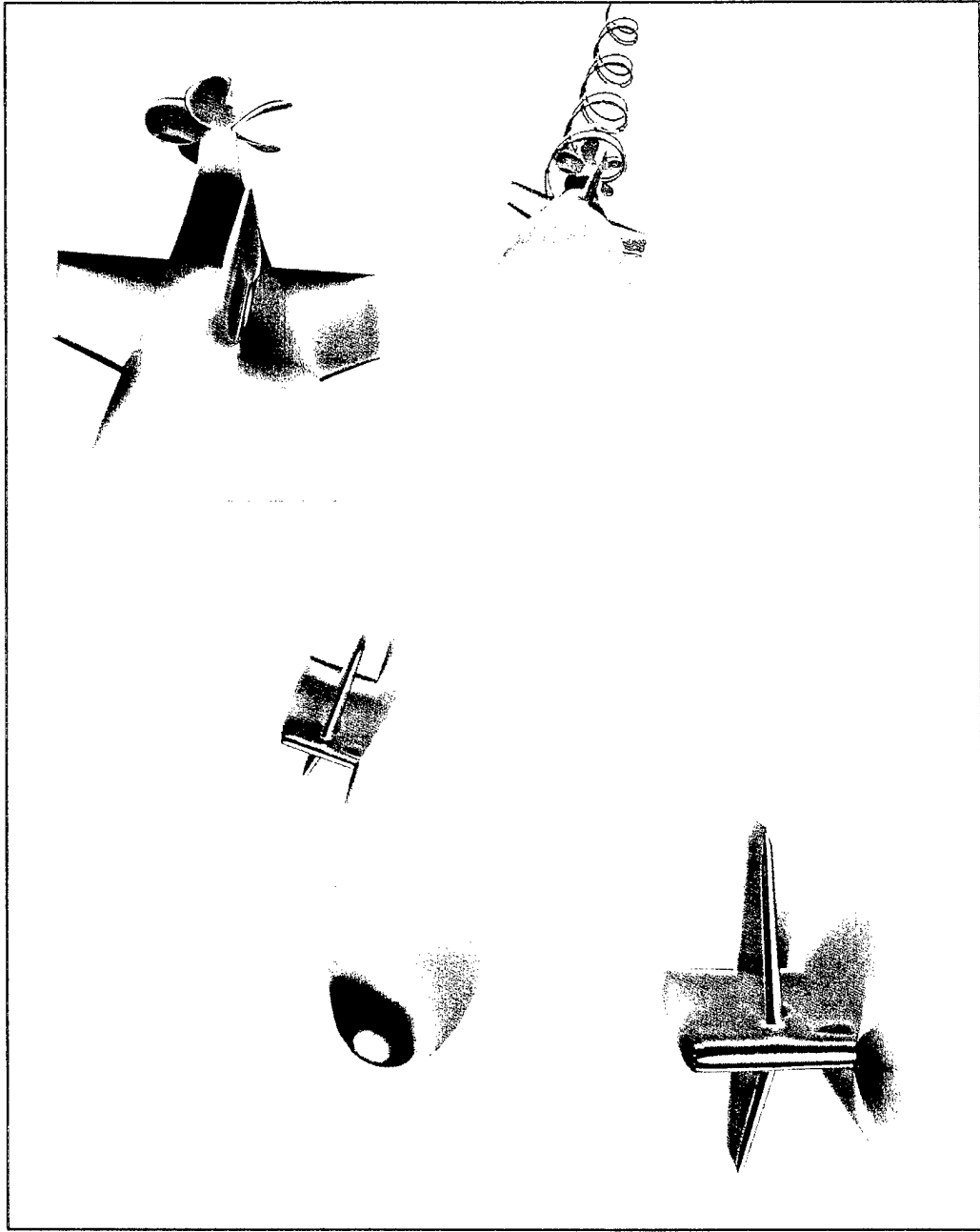
Time history of the rising maneuver

Z-force on top surface of each stern plane and vehicle inertial position

Figure 22.

Figure 23. Pressure distribution during the pitch-up maneuver

Time history of the rising maneuver

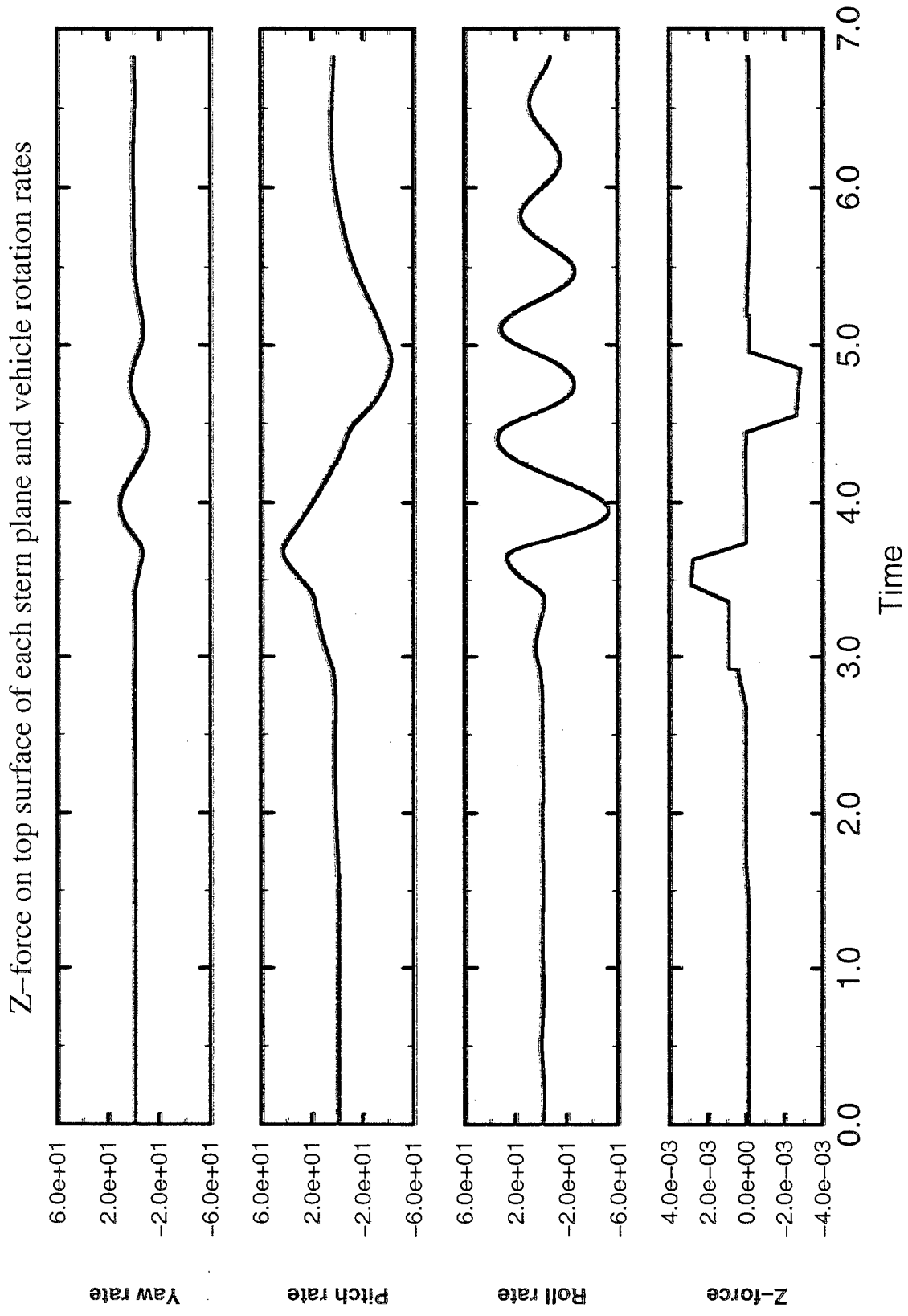Z–force on top surface of each stern plane and vehicle rotation rates

Time

Figure 24.

Time history of the rising maneuver

Z-force on top surface of each stern plane and vehicle inertial orientation

Figure 25.
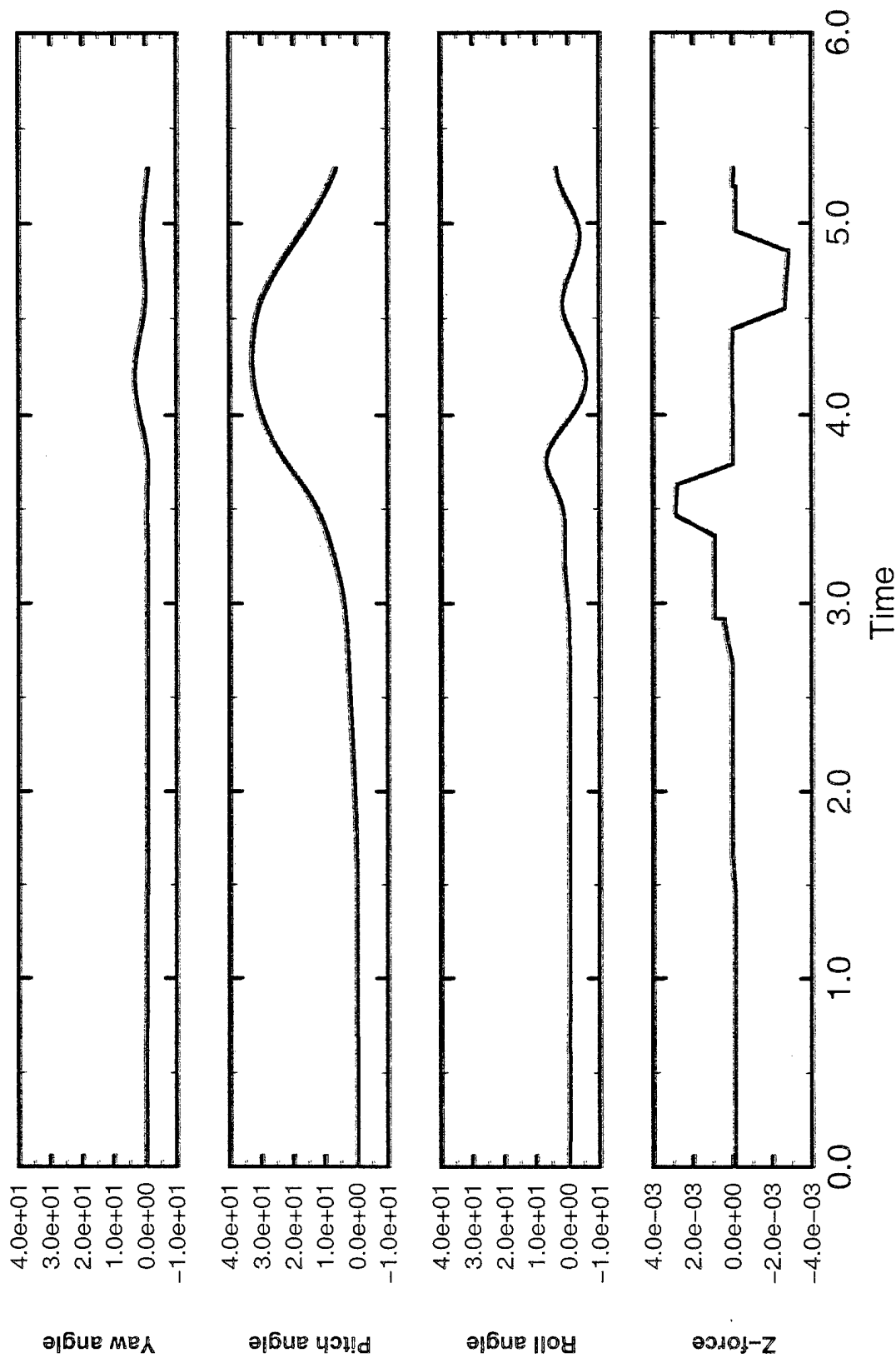
Time history of the diving maneuver

Z-force on bottom surface of each stern plane and vehicle inertial position

Figure 26.

Time history of the diving maneuver
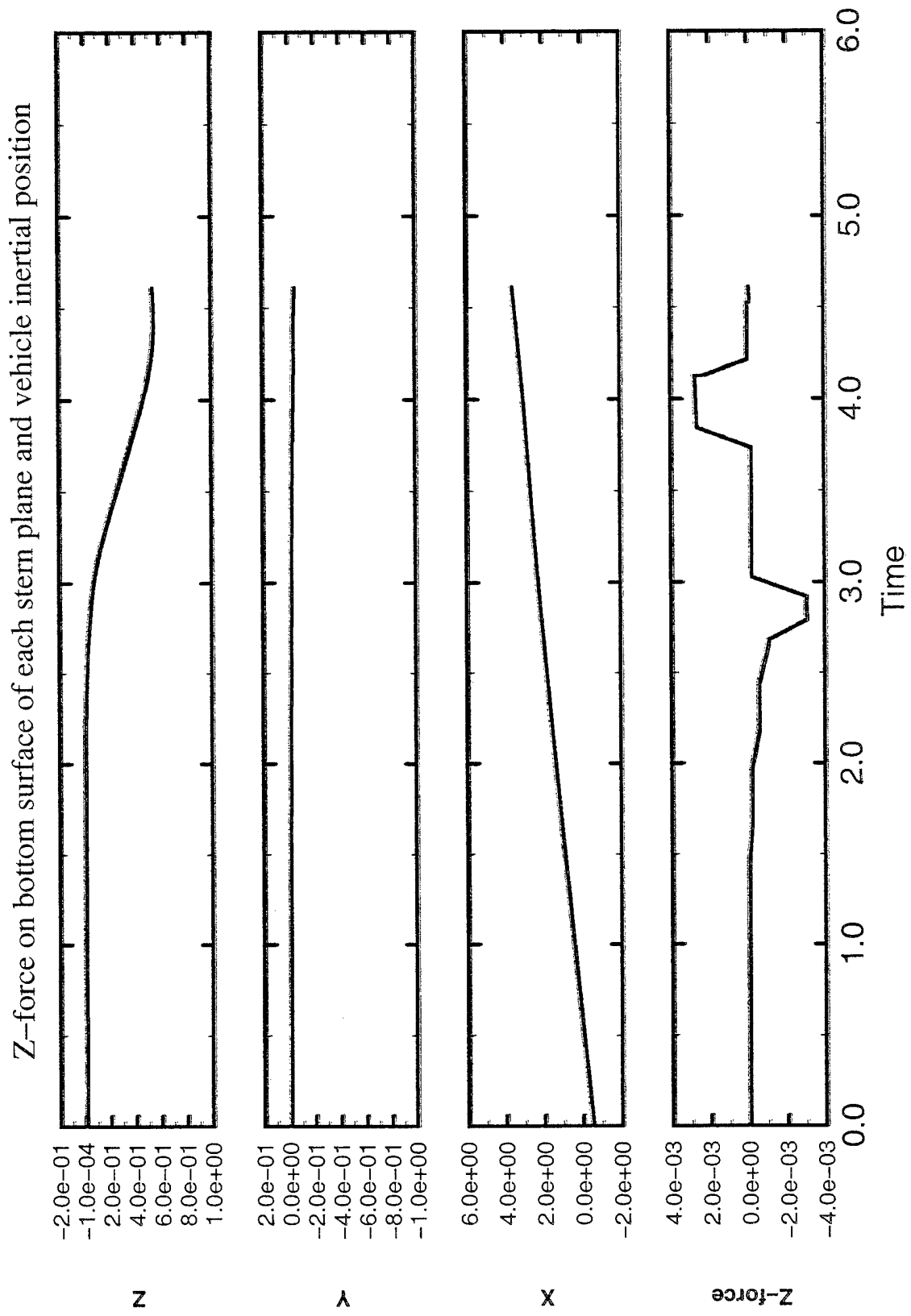
Z–force on bottom surface of each stern plane and vehicle rotation rates
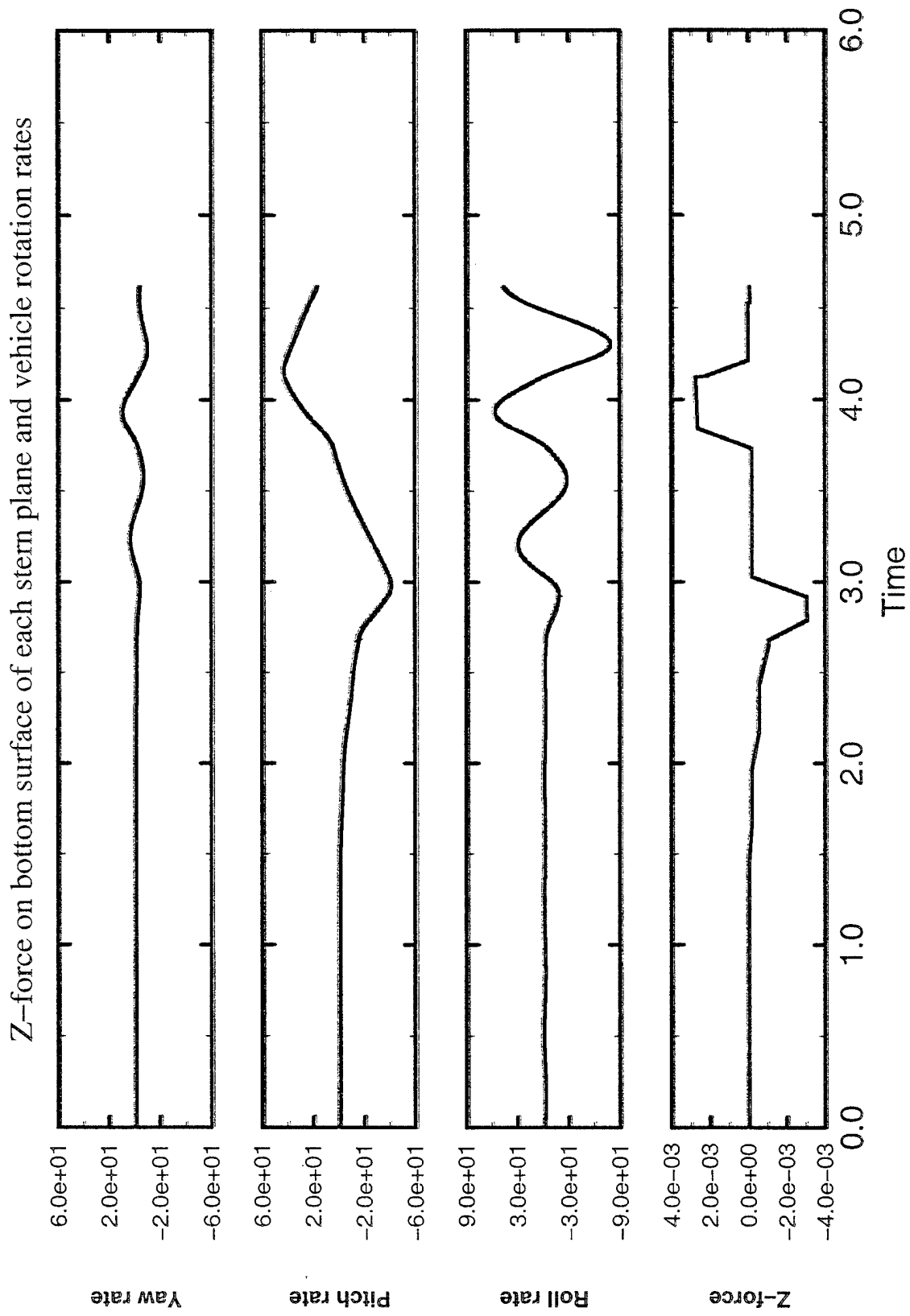
Figure 27.

Time history of the diving maneuver

Z–force on bottom surface of each stern plane and vehicle inertial orientation
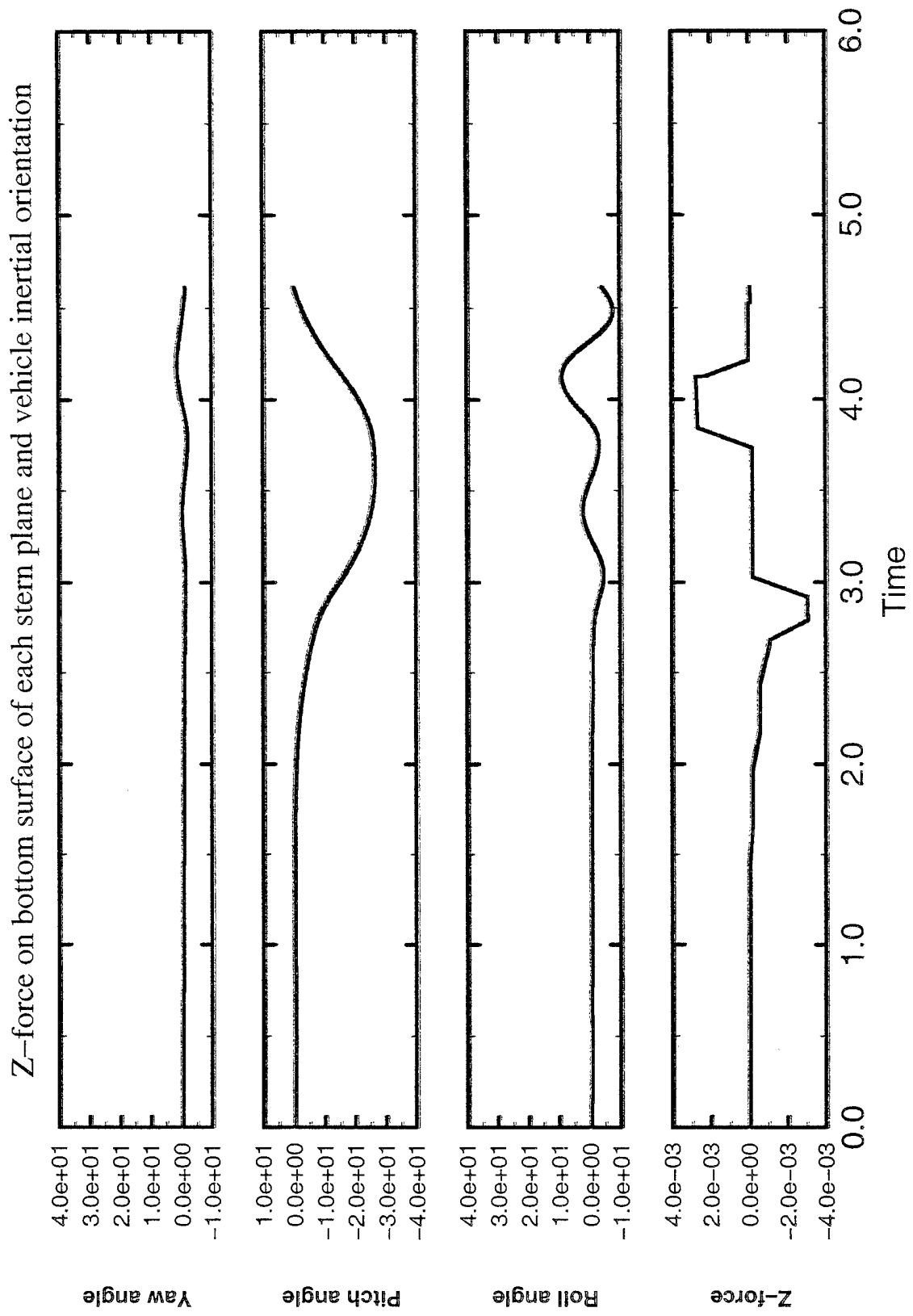
Figure 28.

APPENDIX A

NUMERICAL PREDICTIONS OF TURBULENT FLOWS OVER UNDERWATER VEHICLES AT HIGH INCIDENCE

Farhad Davoudzadeh, David Boger, Howard Gibeling
Computational Mechanics Department
Applied Research Laboratory
The Pennsylvania State University
State College, PA 16804

The high Reynolds number turbulent flow over an appended submarine geometry at high incidence angles is predicted by solving the governing Reynolds-Averaged Navier-Stokes equations. These flowfields are dominated by leeward-side vortical structures and regions of crossflow separation. An algebraic turbulence model as well as various modified versions and a two-equation model are used in several sets of computations. The algebraic model was modified to account for the effects of the leeward-side vortices on the underlying viscous layers. The computed results were compared with experimental data, and advantages and disadvantages of the models are highlighted.

INTRODUCTION

Underwater vehicles and weapons are required to be highly maneuverable. This means flight at high incidence angles. Furthermore, a detailed description of the high incidence flowfield is needed by the designers of the body hull, hull appendages and propulsors. In addition, numerical prediction of the trajectory of the maneuvering bodies requires computations of the high incidence flowfield. McDonald and Whitfield [1] summarized the development of a new physics-based method for the prediction of the trajectory of the underwater vehicles by coupling of the fluid dynamics with the vehicle dynamics. The equations governing the vehicle motion are commonly referred to as the 6DOF equations. The 6DOF equations describe the acceleration of a rigid body given the totality of forces and moments acting on it. The RANS equations provide the means to calculate the hydrodynamic component of these forces and moments. Integration of the 6DOF equations yields the time history of the vehicle's velocity and rotation rate. From this information, the vehicle's trajectory (the history of the position and orientation) can be deduced by integration of purely kinematic relations. Davoudzadeh and others [2] implemented the method and computed trajectories with the coupled solvers for a submarine geometry with a five-bladed propeller. It is clear that the accurate prediction of the forces and moments is key to the accurate prediction of the vehicle trajectory. Therefore, this paper focuses on the accurate prediction of forces and moments acting on underwater vehicles at high incidence, and all of the comparisons made between the computed and the experimental data are for the force components.

The flowfields associated with bodies at high incidence are three-dimensional, turbulent, and contain regions of crossflow separation accompanied by leeward-side vortical structures. Numerical predictions of these flowfields require a very fine grid to capture the off-body vortical structures and to resolve the boundary layer. The off-body vortical structures are essentially inviscid and are created from the underlying turbulent viscous boundary layer. Therefore, the choice of the turbulence model plays a major role on the development, structure, stretching and strength of the vortices. Degani and others [3] introduced a modification to the widely used Baldwin-Lomax eddy-viscosity turbulence model that accounts for the presence of the leeward-side vortex structure. They presented results for supersonic [4] and subsonic [5] high-incidence turbulent flow obtained using a parabolized Navier-Stokes method [6] and their modified turbulence model. They reported good comparisons with the experimental data.

In the current work the models examined are the original Baldwin-Lomax[7], Degani's modified version of the Baldwin-Lomax[3], Baldwin-Lomax with various search parameters, and a new version of the model which has more generality. We also include results using a two-equation turbulence model for comparison. All of the models are incorporated in the incompressible Reynolds-Averaged Navier-Stokes (RANS) code described below.

Implicit Unsteady Incompressible Flow Solver

The three-dimensional unsteady incompressible Reynolds-Averaged Navier-Stokes equations are first written for a time-dependent curvilinear coordinate system. An artificial time term based on the artificial compressibility formulation of Chorin [8] is then introduced to facilitate subiteration at each physical time step (e.g., [9], and [10]). The governing equations are given by

$$\frac{\partial Q}{\partial \tau'} + I_\tau \frac{\partial Q}{\partial \tau} + \frac{\partial F}{\partial \xi} + \frac{\partial G}{\partial \eta} + \frac{\partial H}{\partial \zeta} = 0$$

(1)

where

$$Q = J \begin{bmatrix} p \\ u \\ v \\ w \end{bmatrix}$$

$$K = J \begin{bmatrix} \beta(\theta_k - k_t) \\ u\theta_k + k_x p - T_{k_x} \\ v\theta_k + k_y p - T_{k_y} \\ w\theta_k + k_z p - T_{k_z} \end{bmatrix}$$

$$\theta_k = k_t + k_x u + k_y v + k_z w$$

$$K = F, \theta_k = U \ \text{for} \ k = \xi$$

$$K = G, \theta_k = V \ \text{for} \ k = \eta$$

$$K = H, \theta_k = W \ \text{for} \ k = \zeta$$

In these equations, p is static pressure; u, v, and w are the velocity components in Cartesian coordinates x, y, and z; U, V, and W are the contravariant velocity components in the curvilinear coordinate directions ξ, η, and ζ respectively; and τ is time. The terms $T_{k_x}, T_{k_y}, T_{k_z}$ with $k = \xi$, η, or ζ, are the viscous flux components in curvilinear coordinates. The Jacobian of the inverse transformation is J, and k_x, k_y, k_z, and k_t with $k = \xi$, η, or ζ, are the transformation metric quantities, where a subscript denotes differentiation. The artificial compressibility parameter β typically has a value of 5 to 10. Finally, $I_\tau \equiv \text{diag}\ [0,1,1,1]$, and τ' is an artificial time associated with the subiteration. The first term in Eq. (1) vanishes as the subiteration converges, giving a solution to the physical unsteady equations.

A thin-layer approximation is used to simplify the viscous stress terms, and several turbulence models have been implemented in modular form, including algebraic turbulence models [7], and a q-ω model [11]. Details of treating the viscous terms are given by Gatlin [12], with an improvement due to Chen [13] regarding the computation of tangential velocity derivatives normal to a solid surface. This simple technique works extremely well on highly skewed grids [13].

Equation (1) is first discretized as a cell-centered finite-volume approximation, and the cell-face numerical flux vectors are obtained using Roe's [14] flux difference split scheme. The nonlimited form of the dependent variable extrapolation method of Anderson, Thomas, and van Leer [15] is used to obtain second and third-order flux vectors [15]-[16]. The third-order upwind-biased numerical flux [15] is used for the present results.

The implicit solution procedure for the discretized equations varies according to whether the solution of interest is steady or unsteady. For steady flows, the second term in Eq. (1) is omitted, reducing the equations to a standard artificial compressibility formulation. The spatial difference terms are linearized to produce a linear system for ΔQ^n, which is solved iteratively at each time step [17]. In this case, both ΔQ^n and the steady spatial derivative residuals are zero upon convergence of the (outer) time-step iteration to a steady solution. For unsteady flows, an unsteady residual equation is defined from the last four terms in Eq. (1) and is solved iteratively for Q^{n+1}. In one dimension, for example, the unsteady residual becomes

$$\mathsf{F}(Q^{n+1}) = I_\tau \frac{\Delta Q_i^n}{\Delta \tau} + \delta_i \overline{F}(Q^{n+1}) = 0$$

(2)

The function $\Im(x)$ in (2) is solved by an approximate Newton method given by

$$\mathsf{F}'(Q^{n+1,m})(Q^{n+1,m+1} - Q^{n+1,m}) = \mathsf{F}'(Q^{n+1,m})\Delta Q^{n+1,m} = -\mathsf{F}(Q^{n+1,m})$$

(3)

where m = 1, 2, 3, ... is the Newton iteration index, and $\Im'(x)$ is the Jacobian matrix of the vector $\Im(x)$ modified by replacing I_τ by I to utilize artificial compressibility. In principle, the generated sequence $Q^{n+1, m+1}$ converges to Q^{n+1}, and hence Eq. (2) is satisfied. The linear system for $Q^{n+1 \cdot m+1}$ in Eq. (3) is solved iteratively for each Newton iteration.

A symmetric Gauss-Seidel relaxation is used to solve the linear system of equations associated with each iteration of Eq. (3). Because the flux Jacobian of the flux vector based on Roe's formulation is difficult to obtain analytically in three dimensions, and also in the interest of simplicity, the flux Jacobian is computed numerically [18] [19]. This solution scheme is referred to as a discretized Newton-relaxation [20], or the DNR scheme [19]. A multigrid scheme [21] is used to accelerate the numerical solutions, and this scheme has been extended to multiblock [22] and unsteady flows [23]. The present solution procedure is, therefore, a multigrid scheme for three-dimensional unsteady viscous flow. This procedure is the basis for a flow simulation code called UNCLE (UNsteady Computation of fieLd Equations).

Turbulence Models

Algebraic Models

The well-known Baldwin-Lomax turbulence model, which is based on the two-layer model of Cebeci and others [24], does not take into account the complexities of the three-dimensional flowfield. The model gets particularly confused when local vorticity exists in areas other than the near-wall boundary layer. This situation happens when the flowfield contains vortical structures off of the body. This is due to the fact that the eddy viscosity in the outer region is a function of the magnitude of the local vorticity. In the original Baldwin-Lomax model formulation the algebraic eddy viscosity μ_t is given by:

$$\mu_\tau = \begin{cases} (\mu_t)_{inner}, & y \leq y_c \\ (\mu_t)_{outer}, & y > y_c \end{cases}$$

(4)

where y is the normal distance from the wall and y_c is the smallest value of y at which values from the inner and outer formulas are equal. The Prandtl-Van Driest formulation is used in the inner region

$$(\mu_t)_{inner} = \rho l^2 |\omega| ,$$

(5)

where

$$l = ky [1 - e^{-(y^+/A^-)}];$$

(6)

|ω| is the magnitude of the vorticity

$$|\omega| = \sqrt{\omega_z^2 + \omega_x^2 + \omega_y^2}$$

(7)

and

$$y^+ = (\sqrt{\rho_w \tau_w / \mu_w}) y$$

(8)

In the outer region, for attached boundary layers, the turbulent viscosity coefficient is given by

$$(\mu_t)_{outer} = KC_{cp} \rho\, F_{wake} F_{kleb} (y)$$

(9)

where K is the Clauser constant, C_{cp} is an additional constant and F_{kleb} is the Klebanoff intermittency factor, and

$$F_{wake} = Y_{max}\ F_{max} .$$

(10)

The quantities Y_{max} and F_{max} are derived from the function

$$F(y) = |\omega|\ y [1 - e^{-(y^+/A^+)}]$$

(11)

where F_{max} is the maximum value that the function F(y) takes in a local profile, and Y_{max} is the value at which F_{max} occurs. The constants appearing in the above relationships have been determined by requiring agreement with the Cebeci [24] formulation for constant pressure boundary layers at transonic speeds. The values determined are K = 0.0168, A^+ = 26, and C_{cp} = 1.6.

As previously demonstrated by Degani and Schiff [3] the main difficulty in applying the Baldwin-Lomax turbulence model to three-dimensional flow containing regions of crossflow separation is the determination of the length scale Y_{max} and in turn, of evaluating $(\mu_t)_{outer}$ for boundary-layer profiles in the crossflow separation region. To demonstrate this difficulty, they looked at behavior of the F(y) function along two rays-one located in the windward side at $\phi = \phi_1$ and the other one on the leeward side at $\phi = \phi_2$, shown in Fig. 1. The functions are shown schematically in Figs. 2a and 2b, respectively. The function along the ray in the windward side contains only one well-defined peak, whereas along the ray in the leeward side it contains two distinct peaks. These peaks are manifestations of the vorticity magnitude contained in the function F·(y). The first peak in Fig. 2b comes from the vorticity magnitude contained in the boundary

layer, whereas the second peak originates from the vorticity magnitude contained in the off-wall vortical structure. If one uses the length scale corresponding to this second peak, as would be the case for the original Baldwin-Lomax model, the computed eddy viscosity in Eq. (9) will be at least an order of magnitude larger than the eddy viscosity value related to the length scale corresponding to the first peak. This exaggerated eddy viscosity will have the effect of weakening, deforming, and dissipating, if not eliminating all together, the vortical structures in the flowfield. Furthermore, the computed drag on the body will be too high. This has serious implications on the prediction of the maneuverability of the underwater vehicles with such a model.
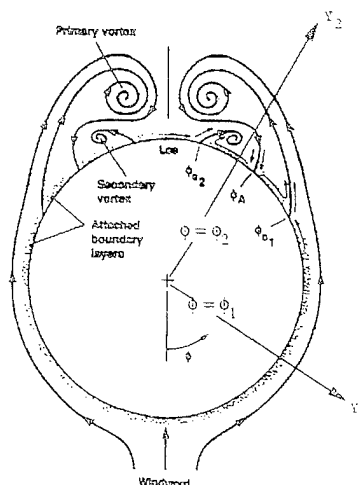
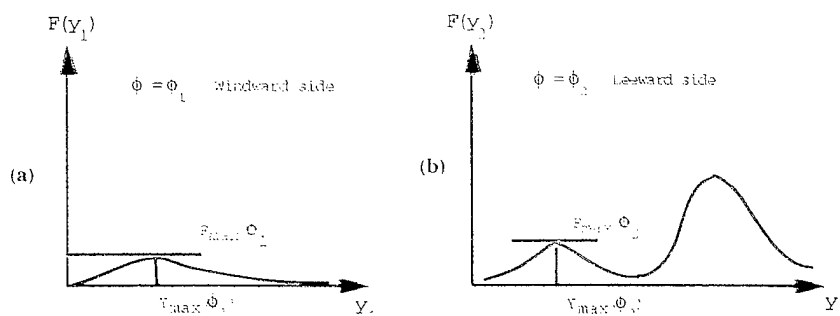Fig 1. Schematic of Flow Structures in Crossflow Plane (After Degani et al. [3])

Fig.2 Behavior of F(y) at Large Incidence at a Cross Section Containing Vortices (After Degani et al. [3])

Partial Differential Turbulence Models

The idea behind eddy viscosity models comes from the Boussinesq approximation that the Reynolds shear stress can be related to the mean shear by

$$-\overline{uv} = v_t \partial U / \partial y.$$

(12)

Equation (12) defines the turbulent viscosity, v_T, which is dimensionally equal to the product of a velocity scale and an appropriate length scale. For example, the Baldwin-Lomax model described above chooses the velocity scale to be the magnitude of vorticity times a length scale, and the length scale is prescribed algebraically. Unfortunately, prescribing a length scale while maintaining sufficient generality is difficult, as was just described.

A method which provides for more generality is to incorporate partial differential equations for the transport, production, and dissipation of both the velocity- and length-scale determining quantities. Here, following Coakley [11], the velocity scale is taken to be the square root of turbulent kinetic energy, q, and the length-scale determining quantity is the time rate of dissipation, ω, governed by

$$\rho\frac{Dq}{Dt} = \frac{\partial}{\partial x_j}\left[\left(\mu+\frac{\mu_T}{\sigma_q}\right)\frac{\partial q}{\partial x_j}\right] + \frac{1}{2q}\left[2\mu_T S_{ij}S_{ij} - \rho\omega q^2\right]$$

$$\rho\frac{D\omega}{Dt} = \frac{\partial}{\partial x_j}\left[\left(\mu+\frac{\mu_T}{\sigma_\omega}\right)\frac{\partial\omega}{\partial x_j}\right] + \rho c_1 c_\mu 2 S_{ij}S_{ij} - \rho c_2\omega^2$$

$$(13)$$

The eddy viscosity is then formulated as

$$\mu_T = \rho c_\mu D q^2 / \omega$$

$$(14)$$

where $D=1-\exp(-\alpha q y/\nu)$ is a damping function based on y, the distance to the nearest solid wall. Completing the model, $\alpha=0.020$, $c_1=0.055+0.5D$, $c_2=0.833$, $c_\mu = 0.09$. and $\sigma_q = \sigma_\omega = 2.0$.

The solution method is the same as the method described previously for the flow equations, except that it is applied to two equations instead of four. The velocity field is treated as known for this part of the solution, but the turbulence equations are coupled together through their source terms. More details of the model and its implementation are described elsewhere [25].

RESULTS

All of the computations presented here are conducted on a SUBOFF body with four stern appendages. SUBOFF has the shape of a typical underwater vehicle. Groves and others [26] designed an axisymmetric hull model for SUBOFF that could be used with and without typical appendage components, such as a fairwater (sail) and four identical stern appendages. Roddy [27] reported experiments that include measurements of forces and moments acting on the SUBOFF body, with and without appendages at drift angles ranging from 0.0° to 18.0°. All experiments were carried out at a Reynolds number of 14.000.000 based on the body length. Since the body is symmetric, only half of the body is gridded for the computations. A C-type grid with 8 blocks and 81x73x33 (195,129) grid points per block--giving a total of 1,561,032 grid points-- is used. The grid is split into two parts in the axial direction and four parts in the circumferential direction. No blocking is made in the radial direction. Each fin surface has 17 grid points in the axial direction and 33 grid points in the radial direction.

Original Baldwin-Lomax

Using the algebraic model as proposed by Baldwin-Lomax [7], a series of steady computations for different drift angles are performed. Fig. 3 shows contours of axial components of vorticity on SUBOFF at 18° angle-of-drift for the computations using the original Baldwin-Lomax model. This figure shows the three dimensionality of the flow, and the development and roll-up of the vortex structure on the leeward side of the body. However, as pointed out earlier, the high value of the calculated eddy viscosity associated with the second peak (see Fig. 2b) causes the vortex to be weak and not well-defined. Fig. 4 shows a cross section of the computed pressure distribution at x/l = 0.63. Fig. 5 shows the axial force against the drift angle, with the error bars associated with the experimental data. The computed axial force, for most angles of drift, underestimates the experimental values, i.e., extra eddy viscosity induces higher drag on the body.
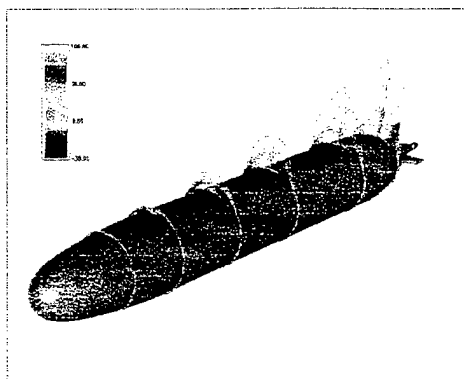
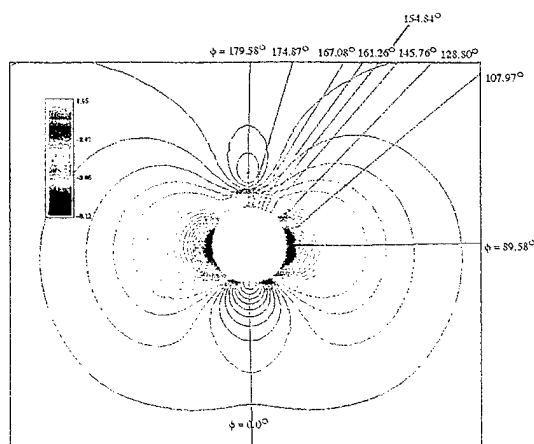Fig. 3 Contours of Axial Component of Vorticity on SUBOFF (Original Baldwin-Lomax, β = 18 deg, Re = 14M)

Fig. 4. Contours of Pressure in the Cross Section at x/L=0.63 (drift angle = 18 deg., Re=14M; Original Baldwin_Lomax
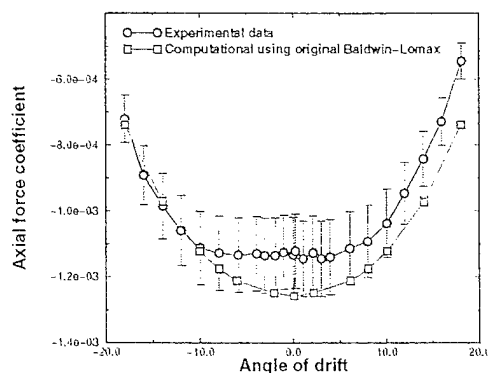

Fig. 5 Computed and Measured Axial Force Coefficient for Various Angles of Drift (Original Baldwin-Lomax)

Baldwin-Lomax with constant search parameter

In the second series of computations, the search for F_{max} along radial rays (shown in Fig.4) is limited to the value $y^+ = 750$. Once this F_{max} is found, the corresponding Y_{max} is determined. Eddy viscosity is subsequently determined from Eqs. 9 and 10. Figure 6 shows the computed contours of the x-component of vorticity for 18.0° angle-of-drift computations. Comparison of this figure with Fig. 3 demonstrates the formation of a stronger and better defined leeward vortical structure. A cross section of pressure distribution at x/l = 0.63 is shown in Fig. 7. In contrast with the Fig. 4, the presence of a pair of very well defined vortices is evident in the leeward side of the body. Figure 7 also shows the radial directions along which the function F is evaluated. The radial lines of 161.26° and 167.08° pass almost through the primary vortex core. A secondary vortex also occurs between the radial lines of 128.8° and 145.76°. Variation of F against y^+, along the radial lines shown in Fig. 7, for 18° drift angle is presented in Fig. 8b. In this figure, the values of F_{max} picked by the computer code, based on the search parameter of 750 are also shown. Figure 8b shows that, for the most part, F_{max} is related to the boundary layer thickness - i.e. the first peak is realized - except at 145.76°. The lower value of F_{max} calculated in this computation results in lower values for the eddy viscosity relative to the original Baldwin-Lomax model. As a result, the leeward vortex is better defined and maintained. Figure 9 shows comparisons of the computed and experimental data for various angles of drift. The model prediction compares well with all the positive angles of drift higher than 10°. The model overpredicts the axial force for drift angles, between 0° and 10°. An examination of the function F along the zero radial line for the zero angle-of-attack cases shown in Fig. 8a, reveals that due to the search constraint of 750, a lower value of F_{max} is picked by the code. This explains why the magnitude of axial force in Fig. 9, for small drift angles is overpredicted. Obviously for small drift angles, one could choose a higher value of the search parameter, but for consistency, all computations presented in Fig. 9 are conducted with the search value of 750.
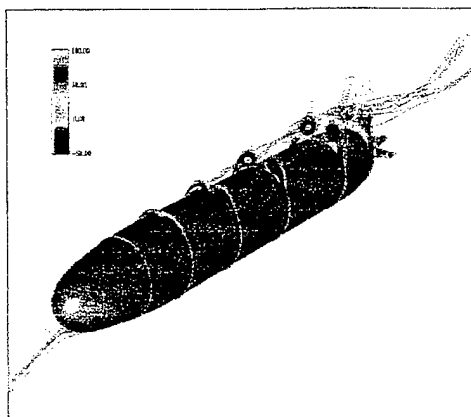
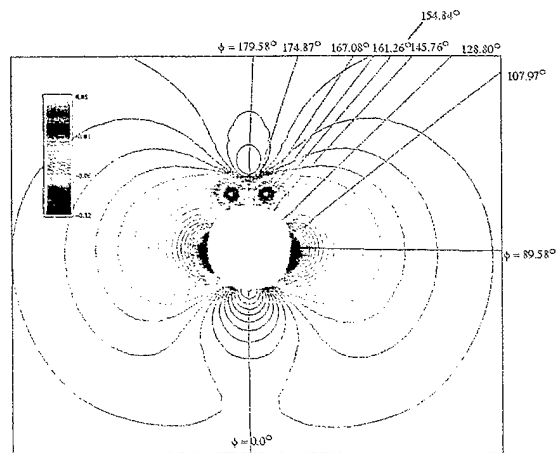Fig. 6 Contours of Axial Component of Vorticity on SUBOFF (Search Parameter = 750, β = 1 8 deg, Re = 14M)

Figure 7. Contours of Pressure in the Cross Section at x/L=0.63 (drift angle = 18 deg. Re = 14M; Baldwin-Lomax with Constant Search Parameter of 750)
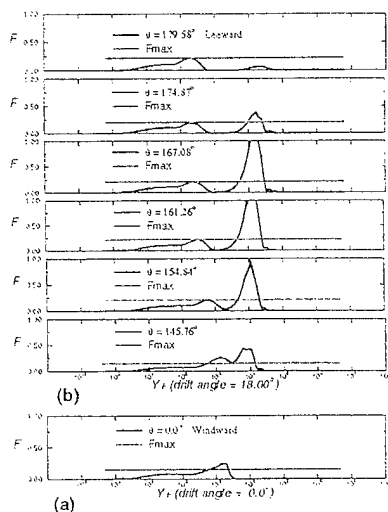

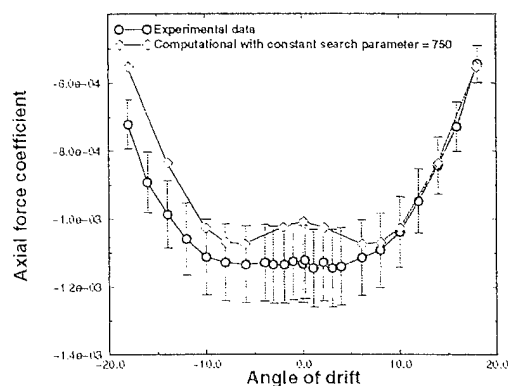Fig. 8 The F as Functions of y^+ Above the Body Surface (Search Parameter = 750)

Fig 9 Computed and Measured Axial Force Coefficient for Various Angles of Drift (Search Parameter = 750)

A close examination of Figs. 8a-8b reveals that a search parameter of $y^+ = 2,500$ is most likely to capture the first peak for all drift angles under consideration. Fig. 10 shows the comparison between the computed axial force coefficient obtained with search parameter of 2,500 and the experimental values at various angles of drift. For drift angles higher than approximately 10°, the comparison is similar to the results obtained with the search parameter of 750. However, for all the angles between 0° and 10°, the prediction is remarkable. Unfortunately, because of the asymmetry of the experimental data (for a symmetric body), no model can predict these experimental data for both negative and positive values of the drift angle. Comparison of the lateral force coefficient is shown in Fig.11. It should be noted that the lateral force coefficients compare well with the experimental data for all of the models discussed above. This is due to the fact that the contribution of the viscous stresses to the computed component of the force is much higher in the axial direction than in the lateral direction. The lateral force comes mainly from the pressure field. This is better demonstrated in Figs. 12 and 13. Figure 12 shows the contributions of the viscous stresses and pressure field to the total axial force coefficient. Figure 12 also shows the total axial force coefficient, both experimental and computed. For drift angles greater than 10°, the pressure field contribution to the axial force creates a thrust on the body (due to the shape anomaly), whereas for drift angles less than 10°, the contribution is drag on the body. Contribution of the viscous stresses to the axial force is all drag. Fig. 13 shows similar divisions for the lateral force coefficient. It is evident from this figure that the contribution of the viscous stresses to the lateral force is very small, compared to pressure.
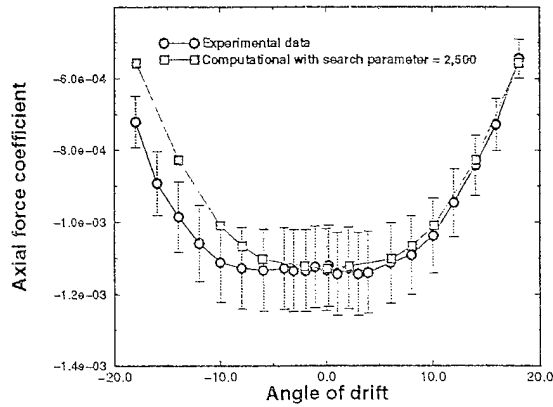
Fig. 10 Computed and Measured Axial Force
Coefficient for Various Angles of Drift (Search
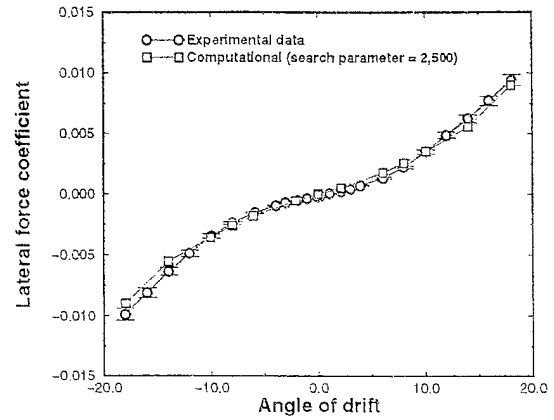Parameter = 2,500)

Fig. 11 Computed & Measured Lateral Force
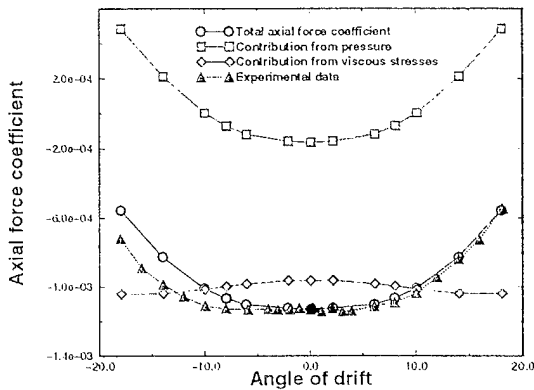Coefficient for Various Angles of Drift
(Search Parameter = 2,500)

Fig. 12 Computed Contribution of Viscous Stresses
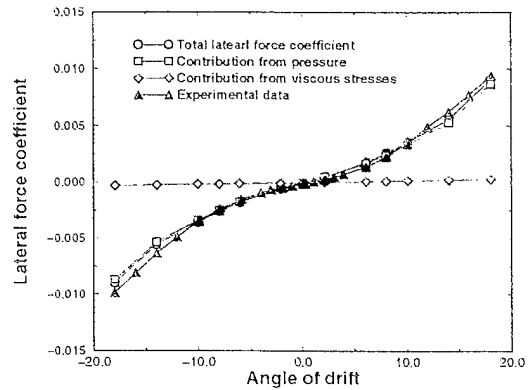& Pressure to the Axial Force Coefficient

Fig. 13 Computed Contribution of Viscous
Stresses and Pressure Field to the Lateral
Force Coefficient

Towards a generalized model

The modified Baldwin-Lomax with the constant search parameter of $y^+ = 2,500$ produces results that compare very well with the experimental data. Choosing an appropriate search parameter in this way relies on trial and error and on running one or two cases, preferably at $0.0°$ and a high degree incidence angle. Degani and Schiff [3] suggested other strategies for setting a search limit which require the prior knowledge of the windward side and the leeward side of the body. The issue with maneuvering bodies is that the windward and the leeward sides are not fixed. The vehicle, in the course of a maneuver, causing a significant change its orientation, causing a change in the locations of the leeward and windward sides.

To eliminate the need for a constant search parameter and the need to know the leeward and the windward sides of the vehicle *a priori*, a new model is suggested. The essence of this new model is that, in the boundary layer, the magnitude of the axial component of vorticity is very small, compared with that of the lateral component of vorticity. Therefore, ω_x does not contribute much to the magnitude of the vorticity in the boundary layer. However, outside of the boundary layer, where the off-body vortex structures exist, the

contribution of the ω_x to the voricity magnitude is large (see Fig. 2b). This implies that ω_x can be used to eliminate the second peak in F by defining a new function G as follows:

$$G(y) = |\overline{\omega}| \, y[1 - e^{-(y^+/A^+)}]$$

(15)

where,

$$|\overline{\omega}| = \sqrt{\omega_z^2 - \omega_x^2 + \omega_y^2}$$

(16)

The functions F and G are shown schematically in Fig. 14. The only difference between the two functions is the way in which $|\overline{\omega}|$ is defined. It is assumed, as shown in Fig. 14a, that G eliminates the second, larger peak produced by F, and that the peak in G occurs at approximately the same y location as the first peak in F. This is a fairly sound assumption, since the contribution of ω_x in the boundary layer to the vorticity magnitude, and therefore the size of the peak, is negligible. Furthermore, since the contribution of ω_x, outside of the boundary layer where vortices exist is large, its exclusion from Eq. (16) can subdue the large peak caused by the vortical structures. For 18.0° angle-of-incidence computations, Fig. 15 shows the variation of different forms of F and G against the radial distance from the wall at $\phi = 167.08°$. Figures 15a-15b and 15c shows F when only the ω_x, ω_y or ω_z were considered in Eq. (7). Figures 15d and 15e show functions G and F. It is clear from Fig. 15a that the magnitude of ω_x is not noticeable in the boundary layer region, and it is very large in the vortex region. Comparison of Fig. 15a with Fig. 15e demonstrates how this large value of ω_x has dominated the overall magnitude of the vorticity and has produced the larger peak in F. On the other hand, Fig. 15d shows how the search for the maximum peak in G yields a length scale that is the same as the first peak in F, Fig. 15e. Using this new modified method a series of computations is performed for incidence angles of 0.0° through 18.0°. Figure 16 shows the pressure distribution at x/l = 0.63 for the drift angle of 18.0°. The leeward vortices are clearly shown on the top portion of the figure. These vortices are stronger and better defined than those obtained under the original Baldwin-Lomax model, but they are not as strong as the ones computed with the constant search parameters. An examination of the variation of F along radial lines, Fig. 17, shows that although the model picks the appropriate peaks for the determination of F_{max} for most rays, it fails for some, e.g. for $\phi = 174.87°$. This deviation occurs because the vortical structures are not aligned with the axial direction of the body, causing the calculated lateral vorticity to have a larger value than the value if the vortex core was aligned with the axis of the body. This causes the shape of G to be different than the assumptions presented earlier. Comparison of the axial force coefficient with the experimental data for this new model is shown in Fig. 18. Unlike the other computations, the computed values fall within the error bars for all positive and negative angles of drift.
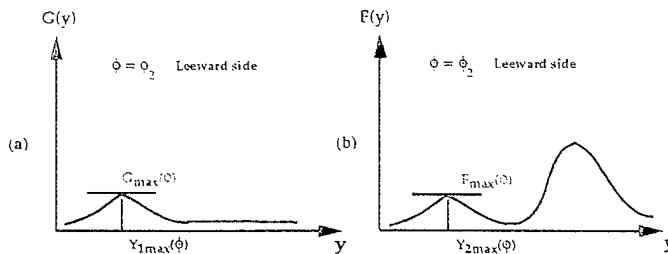
Figs. 14 Behavior of F(x) & G(y) .
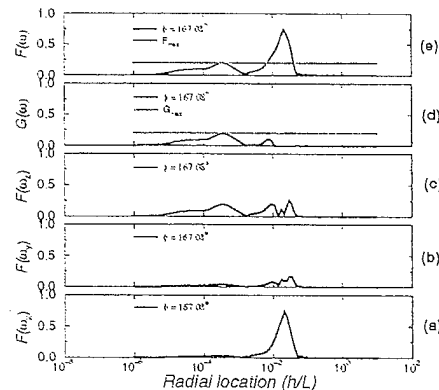
Figs. 15a through 15e Variation of Different Forms of F and G Against the Radial Distance from the Wall at $\theta = 167.08°$
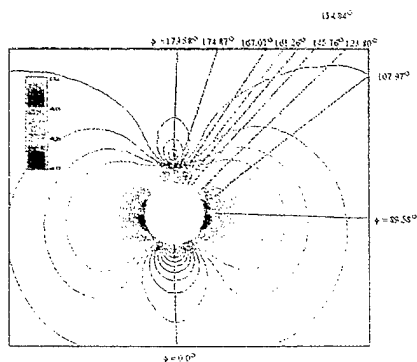
Fig. 16 Contours of Pressure in the Cross Section at x/L=0.63 (Drift Angle=18°, Re=14M, New Model)

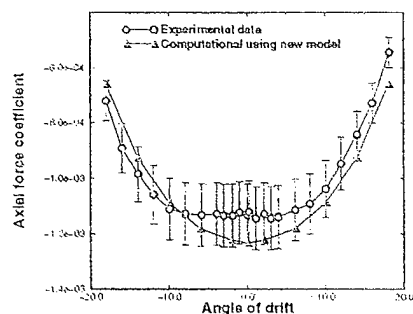Fig. 18 Computed and Measured Axial Force Coefficient for Various Angles of Drift (New Model)

Fig. 17 The F as Functions of Radial Distance Above the Body Surface (New Model)

Two-Equation Model

Algebraic models are highly desirable as turbulence models because they are inexpensive computationally and are generally very robust. On the other hand, higher-order models may be required to attain sufficient generality and accuracy. Here, Coakley's q-ω model was applied to the finest grid for the cases of 0°, 8°, and 18° angle-of-attack. The lateral force was well predicted, similar to the one shown in Figure 11; however, the axial force compared in Fig. 19, is shown to be too high. It was suspected that the cause was an over-prediction of turbulent kinetic energy at stagnation points (principally at the nose). A treatment for this problem has been suggested by Durbin [28], it amounts to the following specified on ω:

$$\omega \geq \sqrt{3(2S_{ij}S_{ij})}C_{\mu}D$$

(17)

The results at 0° and 8° are somewhat improved by this modification, see Fig. 19, but at the cost of robustness - - the case at 18° angle-of-attack could not be completed.

For both two-equation models, the computed eddy viscosity is relatively high in the vortex cores, and consequently, the shed vorticity is diffused too quickly.
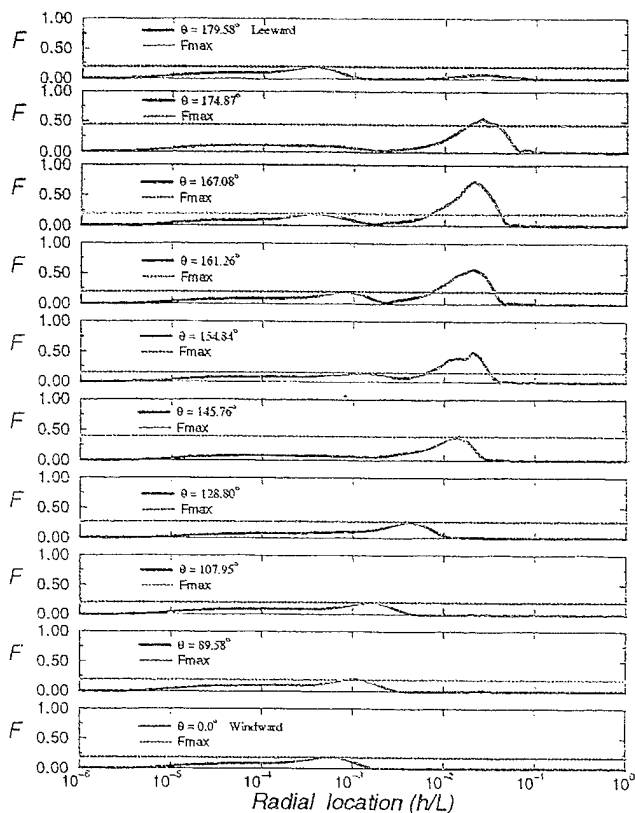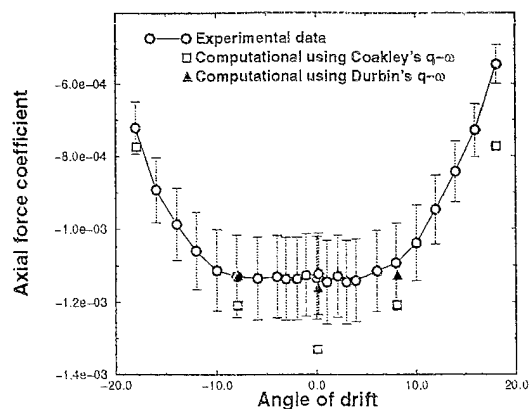
Fig. 19 Computed and Measured Axial Force Coefficient for
Various Angles of Drift (Coakley's and Durbin's q-ω Model)

GRID STUDY

Previously Ref. [25] investigated the influence of grid density on the accuracy of the computed forces and moments, with three grid were constructed: A fine grid with 12 blocks and 81x89x41 grid points per block, a medium grid with 8 blocks, as described earlier, and a coarse grid with 8 blocks and 41x37x17 grid points per block. The results obtained from these three grids considering only the variation of the axial force coefficient with angle of drift showed that only slight differences exist between the fine and medium grids. Computations using the coarse grid under-predict the axial force coefficient for positive angles of drift. All these grids compared well for the lateral force coefficient and yawing moment coefficient. This is due to the fact that the contribution of the viscous stresses to the lateral-force and yawing-moment is not as large as it is for the axial force.

CONCLUSION

A series of computations are performed to evaluate the suitability of several algebraic as well as partial-differential two-equation turbulence models. The algebraic models considered are the original Baldwin-Lomax model, Degani and Schiff variation of the Baldwin-Lomax model, and a new proposed model. Furthermore, the two-equation model of Coakley is also evaluated. The computations demonstrate that the original Baldwin-Lomax is not suitable for the three-dimensional computations that include vortical structure away from the body. This model dissipates and distorts the vortical structures and underestimates axial and lateral forces. The modified Balwin-Lomax with the specified search parameters produces very well-defined vortices, and the computed forces compare well with the experimental data only if a suitable search parameter is used. However, the search for the suitable search parameter relies on trial and error, and therefore, these models are not general. The proposed algebraic model is a general model that does not need a search parameter and does not require prior knowledge of the leeward or the windward side. It preserves the structure of the vortices better than the original Baldwin-Lomax does. However, in its present form, it assumes that the core of the vortical structures is aligned with the axial axis of the body. A more general extension of the model should consider alignment of the vortical structures in any direction. The two- equation model of Coakley is also considered. The model predicts relatively high eddy viscosity in the cores of the shed vortices, and so the vortices diffuse too quickly.

ACKNOWLEDGEMENTS

REFERENCES

1. McDonald, H. and Whitfield, D. L., "Self-Propelled Maneuvering Underwater Vehicles", Presented at the 21st Symposium on Naval Hydrodynamics, Tronheim, Norway, June 24-28, 1996.

2. Davoudzadeh, F., Taylor, L. K., Zierke, W. C. , Dreyer, J. J., McDonald, H., and Whitfield, D. L., "Coupled Navier-Stokes and Equations of Motion Simulation of Submarine Maneuvers, Including Crashback," Presented at the 1997 ASME Fluid Engineering Summer Meeting, Vancouver, British Columbia, Canada, June 22-26, 1997.

3. Degani, D., and Schiff, L. B., "Computation of Turbulent Supersonic Viscous Flows Around Pointed Bodies Having Cross Separation," *Journal of Computational Physics.*, Vol. 66, No. 1, 1986, pp. 173-196.

4. Degani, D., and Schiff, L. B., "Computation of Supersonic Viscous Flows Around Pointed Bodies at Large Incidence," AIAA Paper 83-0034, January 1983.

5. Degani, D., and Levy, Y., "Asymmetric Turbulent Vortical Flows Over Slender Bodies," AIAA Paper 91-3296, September 1991.

6. Schiff, L. B., and Steger, J. L., "Numerical Simulation of Steady Supersonic Viscous Flows," *AIAA Journal*, Vol. 18, No. 12, 1980, pp. 1421-1430.

7. Baldwin, B. S. and Lomax, H., "Thin-Layer Approximation and Algebraic Model for Separated Turbulent Flows," AIAA Paper 78-257, January 1978.

8. Chorin, A. J., "A Numerical Method for Solving Incompressible Viscous Flow Problems," *Journal of Computational Physics*, Vol. 2, 1967, pp. 12-26.

9. Rogers, S. E. and Kwak, D., "Upwind Differencing for the Time-Accurate Incompressible Navier-Stokes Equations," *AIAA Journal*, Vol. 28, No. 2, 1990, pp. 253-262.

10. Taylor, L. K. and Whitfield, D. L., "Unsteady Three-Dimensional Incompressible Euler and Navier-Stokes Solver for Stationary and Dynamic Grids," AIAA Paper 91-1650, 1991.

11. Knight, C. J., and Zajaczkowski, "Validation of a Viscous Incompressible, Throughflow Code," AIAA Paper 95-0864, 33rd Aerospace Sciences Meeting and Exhibit, January 9-12, 1995.

12. Gatlin, B., "An Implicit, Upwind Method for Obtaining Symbiotic Solutions to the Thin-Layer Navier-Stokes Equations," Ph.D. Dissertation, Mississippi State University, August 1987.

13. Chen, J. P., "Unsteady Three-Dimensional Thin-Layer Navier-Stokes Solutions for Turbomachinery in Transonic Flow," Ph.D. Dissertation, Mississippi State University, December 1991.

14. Roe, P. L., "Approximate Riemann Solvers, Parameter Vector, and Difference Schemes," *Journal of Computational Physics*, Vol. 43, 1981, pp. 357-372.

15. Anderson, W. K., Thomas, J. L., and van Leer, B., "Comparison of Finite Volume Flux Vector Splitings for the Euler Equations," *AIAA Journal*, Vol. 24, No. 9, September 1986, pp. 1453-1460.

16. Whitfield, D. L., and Taylor, L. K., "Numerical Solution of the Two-Dimensional Time-Dependent Incompressible Euler Equations," MSSU-EIRS-ERC-93-14, April 1994.

17. Whitfield, D. L., "Newton-Relaxation Schemes for Nonlinear Hyperbolic Systems," Engineering and Industrial Research Station Report MSSU-EIRS-ASE-90-3, Mississippi State University, Mississippi State, MS, October 1990.

18. Whitfield, D. L. and Taylor, L. K., "Discretized Newton-Relaxation Solution of High Resolution Flux-Difference Split Schemes," AIAA Paper 91-1539, 1991.

19. Vanden, K. J., and Whitfield, D. L., "Direct and Iterative Algorithms for the Three-Dimensional Euler Equations," *AIAA Journal*, Vol. 33, No. 5, May 1995, pp. 851-858.

20. Ortega, J. M. and Rheinboldt, W. C., "Iterative Solution of Nonlinear Equations in Several Variables," Academic Press Inc., New York, 1970.

21. Sheng, C., Taylor, L. K., and Whitfield, D. L., "Multigrid Algorithm for Three-Dimensional Incompressible High-Reynolds Number Turbulent Flows," *AIAA Journal*, Vol. 33, No. 11, November 1995, pp. 2073-2079.

22. Sheng, C., Taylor, L. K., "Discretized Newton-Relaxation Solution of High Resolution Flux-Difference Split Schemes," AIAA Paper 91-1539, 1991.

23. Sheng, C., Chen, J. P., Taylor, L. K., Jiang, M. Y., and Whitfield, D. L., "Unsteady Multigrid Method for Simulating 3-D Incompressible Navier-Stokes Flows on Dynamic Relative Motion Grids," AIAA Paper 97-0446, AIAA 35th Aerospace Sciences Meeting and Exhibit, Reno, NV, January 6-10, 1997.

24. Cebeci, T., Smith, A. M. O., and Mosinkis, G., "Calculation of Compressible Adiabatic Turbulent Boundary Layers," *AIAA Journal*, Vol. 8, 1970, pp. 1974-1982.

25. Boger, D. A., Davoudzadeh, F., Dreyer, J. J., McDonald, H., Schott, C. G., Zierke, W. C., Arabshahi, A., Briley, W. R., Busby, J. A., Chen, J. P., Jiang, M. Y., Jonnalagadda, R., McGinley, J., Pankajakshan, R., Sheng, C., Stokes, M. L., Taylor, L. K. and Whitfield, D. S., "A Physics-Based Means of Computing the Flow Around a Maneuvering Underwater Vehicle," Technical Report No. TR 97-002, Applied Research Laboratory, Penn State University, January 1997.

26. Groves, N., Huang, T., Chang, M., "Geometric Characteristics of DARPA SUBOFF Models (DTRC Models 5470 and 5471)," David Taylor Research Center Report SHD-1298-01, March 1989.

27. Roddy, R. F., "Investigation of the Stability and Control Characteristics of Several Configurations of the DARPA SUBOFF Model (DTRC Model 5470) from Captive-Model Experiments," David Taylor Research Center Report DTRC/SHD-1298-08, September 1990.

28. Durbin, P. A., "On the k-ε Stagnation Point Anomaly," *International Journal of Heat and Fluid Flow*, Vol. 17, pp. 89-90, 1996.

29. Coakley, T. J., "Turbulence Modeling Methods for the Compressible Navier-Stokes Equations," AIAA Paper 83-1693.